Pontificia Universidad Católica de Chile
Facultad de Física
Instituto de Astrofísica

Metallicities and Ages in the Red Sequence of Two Clusters of Galaxies.

BY

Constanza Betzabé Muñoz López

Tesis presentada a la Facultad de Física de la Pontificia Universidad Católica de Chile, para optar al Grado Académico de Magíster en Astrofísica.

Supervisor : Dr. Felipe Barrientos
Correctors : Dr. Patricia Tissera
Dr. Médéric Boquien

January, 2022
Santiago, Chile

Declaration

The work described in this thesis was undertaken between 2019 and 2021 while the author was a researcher master student under the supervision of Professor Felipe Barrientos, in the Institute of Astrophysics at Pontificia Universidad Católica de Chile. This work has not been submitted for any other degree at Pontificia Universidad Católica de Chile or any other university.

Para mí, mi familia y amigues

Acknowledgments

Le agradezco a mis padres por la educación que me han entregado durante toda mi vida y por las oportunidades a las que he podido acceder gracias a su apoyo. A mis hermanas y mi sobrina por ser una constante distracción muy necesaria en varias ocaciones. A todos los integrantes de mi familia más cercana, felinos y caninos, gracias por su inconmusurable amor y cariño. También le agradezco a mis amigues y el resto de mi familia más lejana por sus gestos de cariño y compañía.

And I am very thankful as well to Giuseppe D'Ago who helped during the development of my thesis work, thank you for teaching me how to use Ppxf, for your advice, and guidance.

Finalmente, gracias a la Cony del pasado por todo tu arduo trabajo.

Contents

List of Tables

List of Figures

Resumen

Esta tesis se centra principalmente en las propiedades de las galaxias de secuencia roja y qué pueden decirnos estos parámetros acerca de las características y los procesos de formación de las galaxias. Las galaxias de tipo temprano (*early-type*) ofrecen la oportunidad de estudiar la formación y evolución de poblaciones estelares.

Mediante el uso de fotometría proveniente del HST y datos espectroscópicos telescopio VLT/MUSE de dos cúmulos de galaxias, ha sido posible analizar edades y metalicidades de las galaxias y compararlas con otros observables.

Se creó un modelo de secuencia roja para ambos cúmulos y se estableció una conexión entre las edades de las galaxias y sus respectivo desplazamiento con la secuencia roja.

Las observaciones de este trabajo sugieren que la mayoría de las galaxias comenzaron a formar sus poblaciones estelares cuando el Universo era joven ($z > 3$) y que ya tenían acumulada más del 80% de su masa a $z = 2$. Sin embargo, no contamos con la sensibilidad suficiente para establecer el momento exacto en que comenzaron los procesos de formación estelar.

Abstract

This thesis research focuses primarily on the properties of red sequence galaxies and what these parameters can tell us about the characteristics and formation processes of the galaxies. Early-type galaxies offer the opportunity of studying the stellar population formation and evolution.

Using photometry and spectroscopic observational data from HST and VLT/MUSE of two galaxies clusters, we have been able to analyze ages and metallicities of the galaxies as a function of other observable.

We performed a fit for the red sequence in two clusters, and we established a connection between the ages of the galaxies and their respective offset with the red sequence.

The observations in this work suggest that most of the galaxies started to form their stellar population when the Universe was young (z>3) and accumulated more than 80% of their mass at z=2. Nevertheless, we do not have enough sensitivity to set the exact moment when the stellar processes began.

Chapter 1

Introduction

A galaxy is a gravitational bound system of stars, interstellar gas, cosmic dust, and dark matter. Early in the 1900s, the concept of galaxy was not even introduced. In fact, it was just established in the 1920s. Before that time, galaxies were labeled as *nebulae*: of fuzzy appearance with no visual stars seen by telescopes. It was until 1923 that Edwin Hubble calculated the distance to Andromeda 'nebula' (M31), using the 100″ telescope on Mount Wilson, and concluded that M31 was outside the Milky Way, i.e. it is an extragalactic object. Furthermore, he calculated that the distance to Andromeda was at least 300 kpc from the Milky Way. Now we know that the distance is about 800 kpc from our galaxy.

Hubble proposed a classification of galaxies in his book *The Realm of the Nebulae*, in 1936. In this, he recognized three main types of galaxies: ellipticals, lenticulars, and spirals, and a fourth type, irregulars, for those galaxies which did not fit in any of the previous categories. With some modifications and additions, this scheme is still used nowadays (see Fig. 1.1).

Some astronomers hypothesized that the Hubble Sequence was a representation of the life cycle of galaxies, starting their lives from ellipticals to S0s to Sa, Sb, and

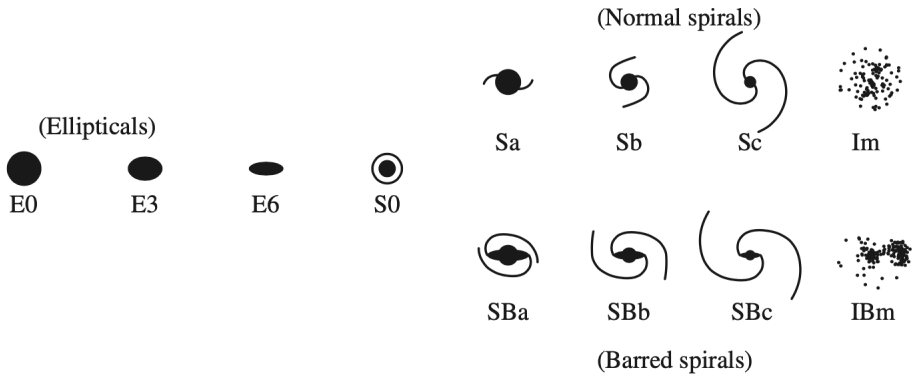

Figure 1.1: Schematic representation of classical Hubble Sequence. 'E' denotes elliptical galaxies, 'S0' lenticular galaxies, 'S' spiral galaxies, and 'I' indicates irregular galaxies. The position in this sequence underlies a link between morphology and galaxy evolution. Image from Abraham (1998).

Sc. They used the terms 'early-type' to named elliptical and lenticular galaxies and 'late-type' to spiral and irregular galaxies. Even though that the hypothesis has been discarded, the terms are still used. Early-type galaxies are essentially quiescent ellipsoidal systems, while late types have a disk with active star formation.

Late-type galaxies are generally bluer in color than early type, primarily due to the presence of hot, young, and massive stellar populations. They typically contain much more gas and dust than early-type, so it is more likely the presence of molecular clouds to have episodes of star formation. Spiral galaxies have flattened disks that are mainly supported by rotation. The rotation of the stars and gas often reveals a spiral pattern that originates the term 'spiral'. On the other hand, elliptical galaxies are supported mainly by the random motions of their stars and have lower gas and dust compared to late-type counterparts. Early-type have not had recent star formation, so the stellar populations are in the majority composed of old stars giving them an appearance redder in the sky. *"Confusingly, 'early- type' galaxies are full of 'late-type' stars, and vice versa."* Sparke & Gallagher (2007).

1.1 Stellar Population of Galaxies

In the majority of galaxies is not possible to resolve individual stars. The observed light of a galaxy is the contribution of the light of all-stars along the line-of-sight (LOS). These stars can differ in properties such as surface temperature, mass, color, size, age, chemical abundances, among others. We will discuss these properties in the next sections.

1.1.1 Stellar Classification

The evolution of a star is mostly determined by its initial mass. Under this consideration, stars can be sorted by the mass content after the main sequence (MS); stars with $M < 8M_{\odot}$ are named red giants and are low-intermediate mass stars that later will evolve into white dwarfs. Stars with $M > 8M_{\odot}$ are known as red supergiants, that in later stages of its lives will explode as supernovae, being able to end up as neutron stars ($1.1M_{\odot} < M_{remnant} < 3M_{\odot}$) or black holes ($M_{remnant} > 3M_{\odot}$), depending on the mass of the supernova remnant.

The Hertzsprung–Russell diagram or HR diagram (Fig. 1.2) allows us to define unlike stellar phases. How much time stars spend in the main sequence phase depends on their initial mass, with a lifetime scale in the MS of $\sim \tau \propto M^{-3}$. The HR diagram contains vast and varied information regarding stars and stellar populations. To have a better understanding of the diagram, we will review some concepts.

The Stefan-Boltzmann relation establishes a connection between T_{eff}, luminosity L, and radius R of a star, meaning that more luminous stars have a larger radius than less bright stars at the same temperature. As well, the mass-luminosity relation (Kuiper (1938)), $L \propto M^{3.5}$, set up that mass and luminosity are related, with more massive stars being more luminous.

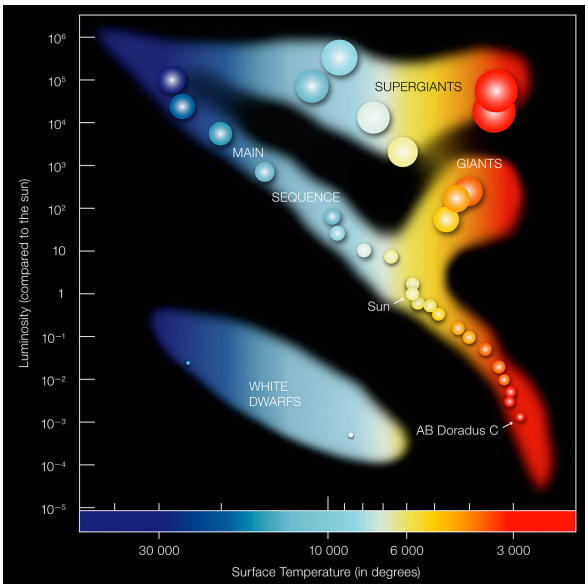

Figure 1.2: Hertzsprung–Russell or HR diagram with the surface temperature and color index in the x-axis and luminosity in the y-axis. From the diagram is possible to infer that the main sequence can go from hot, luminous, blue O type stars to cool, faint, red M stars. (Source: eso.org)

In this context, it is possible to classify stars according to the surface temperature, as the Morgan-Keenan (MK) system does it (Morgan et al. (1943)). Early-type stars (O, B, A, F) have T_{eff} ranging from 50000 K to 7000 K, they are more luminous (L> $1.5L_{\odot}$ up to over $10^4 L_{\odot}$), bigger with radius from $1.15R_{\odot}$ up to over $10R_{\odot}$, more massive ($1.4M_{\odot}$ up to over $80M_{\odot}$) and appear bluer (B-V> 0.5) in a HR diagram (Fig. 1.2), compared to late-type stars. On the other hand, late-type stars (G, K, M) have T_{eff} ranging from 7000 K to 3500 K, luminosity of L< $1.5L_{\odot}$ down to below $0.08L_{\odot}$, redder colors (B-V)< 0.5, sizes from $1.15R_{\odot}$ down to below $0.7R_{\odot}$, and low masses ranging from 0.08 to $1.4M_{\odot}$.

We will note distinct features if we observe the spectrum of stars classified according to the MK system. O, B stars have strong absorption lines of HeII, HeI, and ionized species, with a strong UV continuum. A, F stars show an increment in the intensity of metals and CaII lines, with H lines decreasing in strength from A to F stars. In the

case of G, K, and M stars, there is a strong presence of metal lines, for example, Mg, Na, and the CaII; and molecular bands, such as TiO (Leveque (2017)). There is also strong emission in the optical red and the near-infrared and a weak blue continuum (see Fig. 1.3).

1.1.2 Types of Stellar Population

A stellar population can be characterized by its star-formation history (SFH: $\psi(t)$), an initial mass function (IMF: $\varphi(m)$), and its history of chemical enrichment.

A Simple Stellar Population (SSP) is an assembly of stars born in the same star formation event; this means that they are coeval and share the same chemical composition at the beginning of their lives. As we know, the evolution of a star is determined by its mass; in this way, the number and the type of stars that make up an SSP will change with time, varying the properties of the stellar population. So at each time, the SSP is composed of a different number of stars associated with the IMF. These stars are at different stellar phases, which is related to the isochrone (Leveque (2017)), and have different masses, so they fall in a different part of the HR diagram.

A Complex Stellar Population (CSP) can describe a galaxy that has undergone different star-forming processes. This scenario can be pictured as the galaxy's stellar population is composed of individual SSP, each of them weighted by the star formation rate (SFR: stellar mass formed per year). SFR tells us the number of star-forming processes experienced recently by a galaxy (10 - 100 Myr). The SFR is not always constant in time; it can change with time. This change is given by the star formation history (SFH). In general, the SFH of an elliptical galaxy follows a decreasing exponential function, and in spiral galaxies is assumed to be constant (Schmidt (1959), Kennicutt (1998))

Elliptical galaxies have small ongoing star formation, with spectral properties (e.g., colors and absorption line indices) that can be well fitted by a simple single-age stellar population. Their spectra show strong emission in the IR, consistent with that almost all the massive stars have already evolved. Disk galaxies, otherwise, usually have significant ongoing star formation. Their star-formation histories, 'modeled' as declining exponentially in the function of time, are inconsistent with a single burst (Tremonti et al. (2004)). A CSP better describes its stellar population. Moreover, their spectra present high emissions in the UV region due to new young stars.

If one assumes a universal IMF in elliptical galaxies, it is possible to find constraints in the SFHs. There are two approaches: the archaeological method, in which the IMF is inferred from the observable properties of nowadays ellipticals, and the evolutionary approach, where the IMF can be studied from the observed properties of ellipticals at different redshifts.

1.2 Early-type Galaxies

As it was explained early, galaxies can be separated into two main groups if we describe their light distribution: early-type galaxies (elliptical and lenticular galaxies) and late-type galaxies (spiral and irregular galaxies).

Elliptical galaxies are described as smooth, elliptical surface brightness distributions and some featureless, generally lacking in cool gas or dust, which means that they contain few young blue stars, giving them photometric red colors, distinctive of old stellar populations ('late-type' stars).

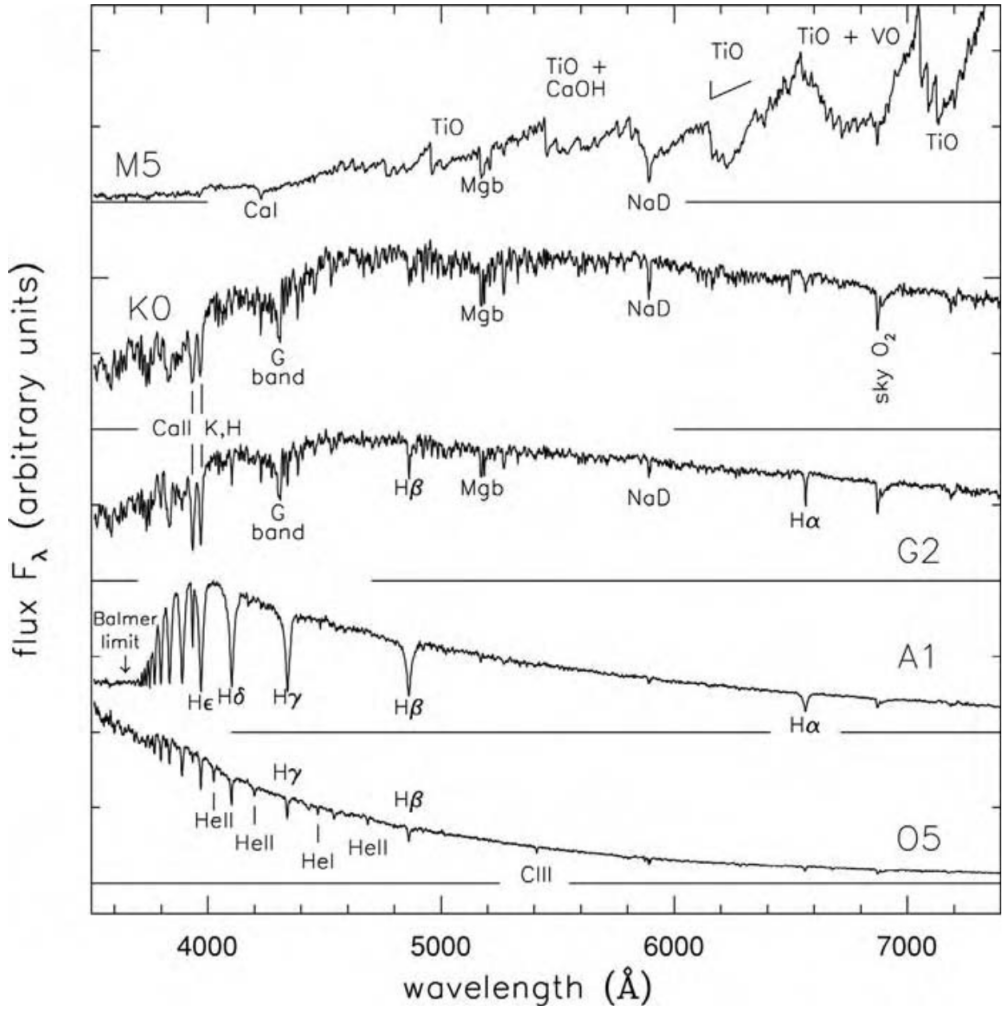

Figure 1.3: Optical spectra from stars in the main sequence, with metallicity close to solar. Surface temperature decreases from bottom to top; the spectral classes appear in the corner of each spectrum. Image from Sparke & Gallagher (2007).

1.2.1 Early-type Galaxies Properties

Elliptical galaxies are the most luminous galaxies in the Universe but also the dimmest. Luminous giant ellipticals can have $L >\sim 2\times10^{10}L_{\odot}$, equal to blue magnitude $M_B \approx$ -20. Midsized ellipticals are less luminous, with luminosities $L > 3\times10^{9}L_{\odot}$, equivalent to $M_B \lesssim$ -18. Ultimately Dwarf elliptical are those with $L < 3\times10^{9}L_{\odot}$. Isophotes or contours of constant surface brightness allow classifying elliptical galaxies by the Hubble type E#, where #= 10(1-b/a)= 10(1-q)= 10ϵ, being a,b, and ϵ the ratio of the semi-major axis, the semi-minor axis b and the ellipticity of the ellipse. '#' is not an intrinsic parameter of the ellipse but a projection of the inclination angle with respect to our line-of-sight.

In general luminous elliptical are classified as E1-E2 (<q>= 0.85), very few circular or E0 ($q \sim$1). They also have high Sèrsic index (n), triaxial ellipsoids, boxy isophotes, flat nuclear profiles, and anisotropic velocities. Midsize ellipticals have an apparent axis ratio q≈ 0.75 corresponding to E2.5, lower Sèrsic index n, the morphology of oblate spheroids, disky isophotes, steep nuclear profiles, and isotropic velocities. Dwarf elliptical (dE and DSph) present smooth light distribution and no disk, but exponential profiles (n= 1) and they do not follow elliptical parameter correlations.

Lenticular galaxies are in a transition between elliptical and spiral galaxies. They present intermediate morphology: central bulge, disk steeply declining in brightness, and no spiral structure. These galaxies present low gas in the interstellar medium, so low young stars. In the Hubble scheme, they are classified as S0 or SB0 (barred lenticular).

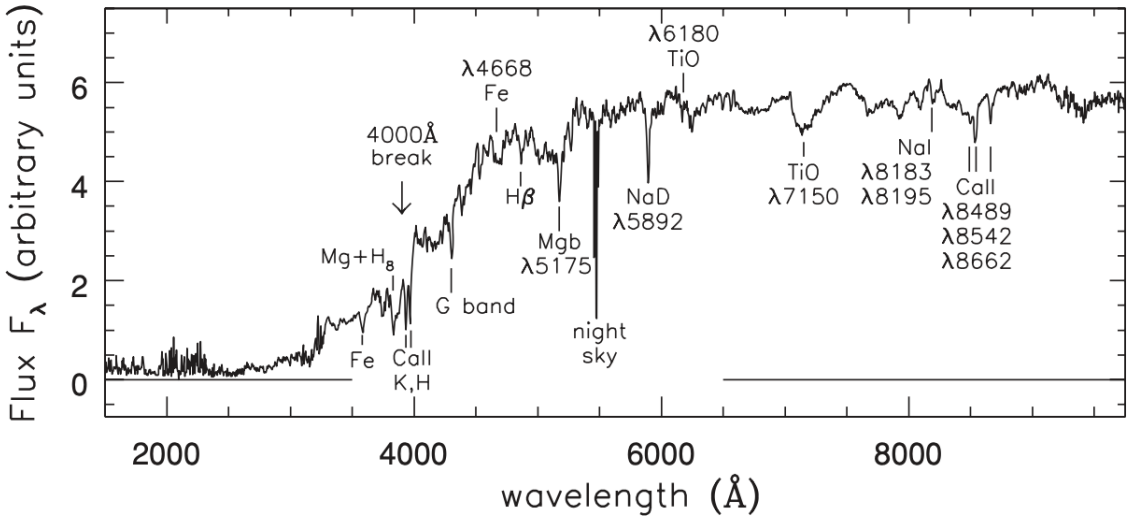

Figure 1.4: Spectrum of an elliptical galaxy with typical features (absorption lines). Image from Sparke & Gallagher (2007).

1.2.2 Stellar Population of Elliptical Galaxies

Elliptical galaxies lack bright blue stars; in their case, the most luminous stars are red giants and stars on the asymptotic giant branch (AGB). Even in the nearest ellipticals, it is impossible to resolve stars, so the light of AGB stars and those around the tip of the red giant branch are the ones that in the majority contribute to observations. Fig. 1.4 corresponds to the typical spectrum of an elliptical galaxy, it shows deep absorption lines of calcium and magnesium, alike to the K-star in Fig. 1.3. The small fraction of light below 3500Å is a sign that the galaxy has made few stars in the last 2 Gyr (from analysis using Geneva Observatory tracks). The break at 4000Å comes from the metal absorption at short wavelengths and from the lack of hot blue stars as well.

1.2.3 Red Sequence

In Fig. 1.3 we can see that more massive stars (O, A-type) emit more fraction of their light at low wavelengths compared with low-mass star (M type). In general, the lifetime of massive stars is short; therefore, the color distribution of a galaxy contains

key details about the star-formation history. However, other factors affect the color of a galaxy, which can make them appear redder, such as the stars' metallicity; stars with high metallicity tend to be redder. The presence of dust also affects the color of a galaxy since the dust extinction is more effective at short wavelengths.

Fig. 1.5 shows the color distribution of ~365,000 galaxies in the SDSS. As seen in the figure, the shape of the probability density corresponds to a bimodal distribution with two peaks, one at the red part and the other at the blue part, being the last one broader. This represents basically that galaxies are distributed in two main groups: early-type galaxies containing old population thus red colors, and late-type galaxies with active star formation in their disks, consequently young stars which gives them bluer colors. Nonetheless, elliptical galaxies can have been through recent star formation events and appear less red, just as disk galaxies can contain a large fraction of dust and look less blue. Consequently, the galaxy population at the bright end of the bimodal distribution is known as the red sequence. On the other hand, the faint end is mostly dominated by blue galaxies, usually called blue sequence or blue cloud.

So the *red sequence* is dominated by early-type or elliptical/ lenticular galaxies. The color of these galaxies is consistent with their stellar population being old and metal-rich. The research presented in this thesis consisted in elucidating which of these two effects dominates. To reach this goal, we analyzed two clusters of galaxies: RXJ1347 and RCS0327.

1.3 Clusters of Galaxies

Clusters of galaxies are the most massive gravitationally-bound structures in the Universe and excellent target to study the evolution of the galaxies population. The mass of a cluster is composed by: $\sim 90\%$ dark matter, the Intracluster Medium (ICM) $\sim 9\%$ and galaxies $\sim 1\%$. In general, clusters of galaxies are rich in early-type galaxies;

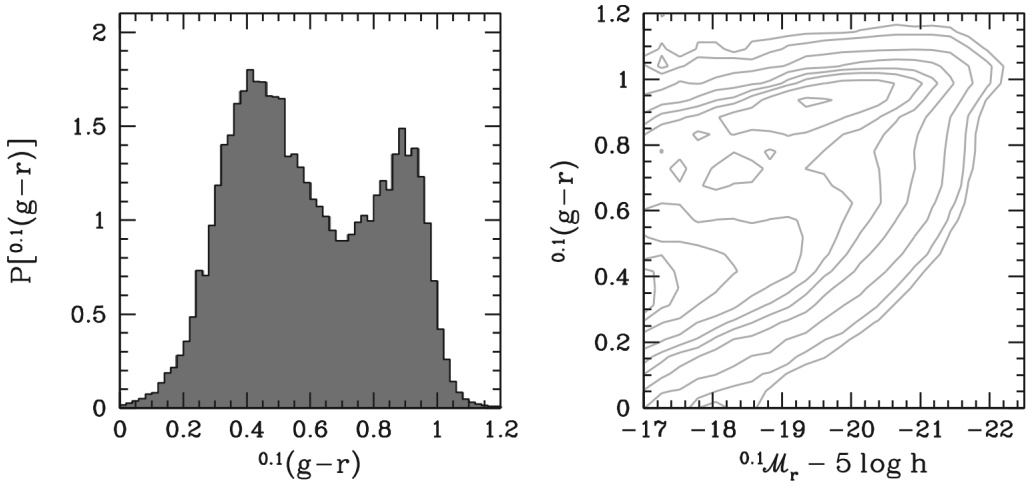

Figure 1.5: Probability density of colors in the left and color-magnitude diagram in the right of ~365,000 galaxies from the SDSS. Superscript points out that the magnitudes have been shifted to the same rest-frame wavebands at z= 0.1. The sample has been corrected for Malmquist bias. Image from Mo et al. (2010).

in regular clusters, E+S0 galaxies can represent ~ 80% of the total population, ~ 50% in irregular clusters, and ~ 30% in the regular field Tremonti et al. (2004).

Galaxies are principally found in dense regions of the Universe, called clusters of galaxies. Catalogs proposed by Abell (Abell (1958)) and Zwicky (Zwicky et al. (1961)) are two essential catalogs of clusters of galaxies.

1.3.1 Properties of Clusters of Galaxies

There are different definitions of a cluster of galaxies. One of these is galaxies in a specific region of the sky, with velocity within the observed velocity dispersion range. This definition affects the number of member galaxies. Generally, a cluster has a diameter from 2 - 10 Mpc; how many galaxies are inside this region measures a cluster's richness.

Abell defined the richness of a cluster as independent of the distance. A galaxy is

a member of the cluster if its apparent magnitude is between m_3 and m_3+2, being m_3 the apparent magnitude of the third brightest member. This lead to the Abell radius, defined as 15 $h^{-1}Mpc$ ($h=\frac{H_0}{100}$, $H_0=100\ km\,s^{-1}Mpc^{-1}$, the Hubble constant). Galaxies within the Abell radius are members of the cluster, this tell how compact is a cluster. A poor cluster has around 30-50 members.

Abell distinguishes between two morphological types of clusters: regular and irregular. The first type has a spherical shape with a high concentration of galaxies in the central part, suggesting, in some cases, a relaxed dynamical system. On the other hand, irregular clusters present low central concentration, usually presenting sub clustering. In terms of dynamics, these clusters are less evolved and have had a similar distribution of galaxies since their formation.

Chapter 2

Observations and Data Processing

In this research, we worked with images of the clusters RXJ1347.5-1145 and RCS0327-1326 in different filters taken by the *Hubble Space Telescope* (HST) and spectroscopic data of both clusters taken by the spectrograph *Multi-Unit Spectroscopic Explorer* (MUSE) installed at the Very Large Telescope (VLT).

2.1 Cluster Basic Information

2.1.1 RXJ1347.5-1145

RXJ1347-1145 at z= 0.451, is one of the most luminous cluster in X-ray. This cluster of galaxies was observed for the first time with ROSAT in X-Rays (Schindler et al. (1995)) and later with the X-ray satellites, *Chandra* (Allen et al. (2003); Bradač et al. (2008)), *XMM-Newton* (Gitti (2004)), and *Suzaku* (Ota, N. et al. (2008)). Studies with high-resolution imaging and spectral observation, had found a non-isotropic temperature distribution and two hot regions (kT> 20eV) as result of its gas content.

Images taken by the Very Large Array (VLA) indicate that the core of RXJ1347 shows extended emission in radio, with radio flux density equal to 25.2 ± 0.3 mJy (Gitti,

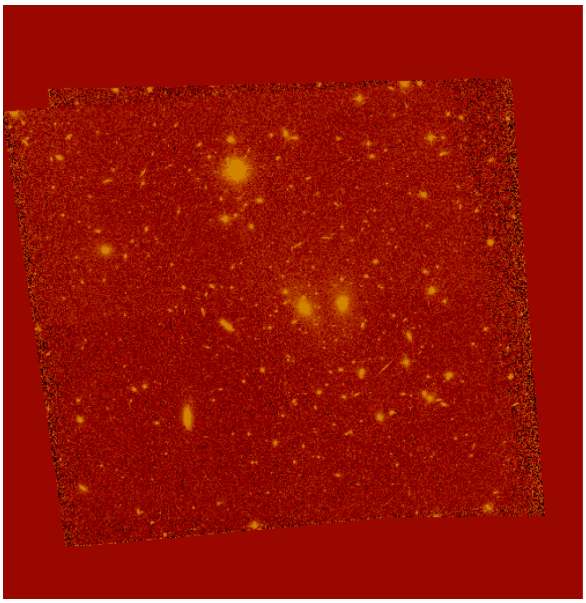

Figure 2.1: RXJ1347 image taken by ACS from HST in the F814W filter. The instrumental aperture used was WFC-Fix.

M. et al. (2007)).

Optical observations of RXJ1347 have confirmed that the number of galaxies members are ~140 through redshift analysis (Lu et al. (2010), Cohen & Kneib (2001)).

Fig. 2.1 shows an image of the cluster RXJ1347 used in this work.

2.1.2 RCS0327-1326

The Red Sequence Cluster Survey is a project created to identify galaxy clusters at different redshifts. The project was originally performed (from 1999 to 2001) using in the northern hemisphere the Canada- France-Hawaii 3.6 m telescope and in the southern hemisphere the Cerro Tololo Inter-American Observatory 4 m telescope (Gladders & Yee (2001)). Later, ESO Very Large Telescope followed up some of the clusters in the sample.

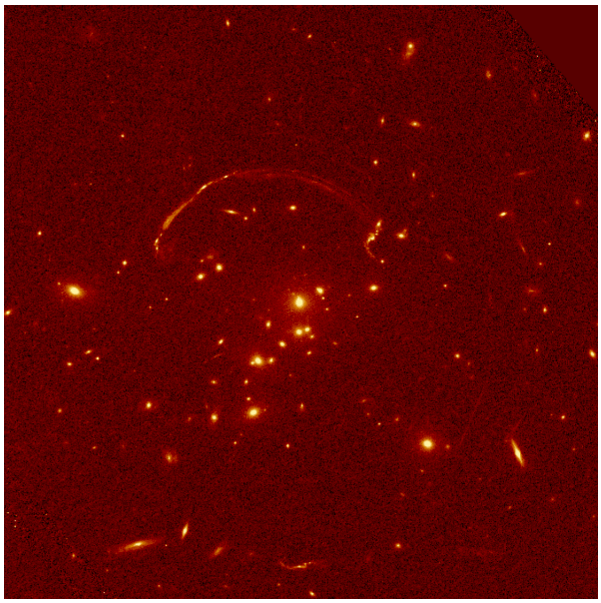

Figure 2.2: RCS0327 image taken by WFC3 from HST in the F814W filter. The instrumental aperture used was UVIS1.

RCS0327-1327 was identified by the second Red Sequence Cluster Survey (RCS2). The foreground galaxy cluster that acts as the lens of the system is located at z= 0.564. In images of the cluster, it is possible to appreciate giant arcs extended over ~ 38", which were reported for the first time in 2010 (Wuyts et al. (2010)). These are the results of the lensing of the background galaxy RCSGA 0327-132609 at z= 1.704, which is one of the best-studied star-forming galaxies at high redshift.

Previous works have identify ~44 galaxies cluster member in RCS0327 (Carrasco et al. (2017)), in a field-of-view of 75"x75", using images from thee RCS2 survey.

Fig. 2.2 shows an image of the cluster RCS0327 cluster used in this work.

Filter	Wavelength Range [Å]	Tel.	Inst.	Image Type	Obs-Type	Obs-Mode	Detector	Aperture	Exp-Time [s]	Date-Obs
F475W	3858 - 5560	HST	ACS	EXT	IMAGING	ACCUM	WFC	WFC-FIX	10560	2006-03-11
F814W	6867 - 9626	HST	ACS	EXT	IMAGING	ACCUM	WFC	WFC-FIX	14680	2006-03-10
F125W	10844 - 14139	HST	WFC3	EXT	IMAGING	MULTIACCUM	IR	IR-FIX	2414	2011-04-20

Table 2.1: Data and instrument information for RXJ1347 images. Tel., Inst., Image Type, Obs-Type., Obs-Mode, Detector, Aperture, Exp-Time and Data-Obs, denotes the telescope and instrument to acquire the data, the type of exposure identifier, the observation type, the operating mode, the detector used, the aperture, the exposure duration (calculated), and the date when the observations were realized, respectively.

Filter	Wavelength Range [Å]	Tel.	Inst.	Image Type	Obs-Type	Obs-Mode	Detector	Aperture	Exp-Time [s]	Date-Observed
F606W	4646 - 7179	HST	WFC3	EXT	IMAGING	ACCUM	UVIS	UVIS1	1003	2011-03-01
F814W	6867 - 9626	HST	WFC3	EXT	IMAGING	ACCUM	UVIS	UVIS1	2133	2011-03-01
F160W	13854 - 17000	HST	WFC3	EXT	IMAGING	MULTIACCUM	IR	IR-FIX	862	2011-03-01

Table 2.2: Data and instrument information for RCS0327 images. Tel., Inst., Image Type, Obs-Type., Obs-Mode, Detector, Aperture, Exp-Time and Data-Obs, denotes the telescope and instrument to acquire the data, the type of exposure identifier, the observation type, the operating mode, the detector used, the aperture, the exposure duration (calculated), and the date when the observations were realized, respectively.

2.2 HST Photometry

For RXJ1347, we used photometry data in three filters from the HST: F475W, F814W, and F125W. Table 2.1 shows the primary information of the images used in this thesis for the cluster.

For RCS0327, we used photometry data in three filters from the HST: F606W, F814W, and F160W. Table 2.2 shows the primary information of the images used in this thesis for this cluster.

2.2.1 HST Field-of-view

Images from the HST instrument WFC3 (Wide Field Camera 3) are subject to geometric distortion due to the tilt of the focal plane with respect to the optical axis, which causes elongation of the field of view. For this reason, the field of the detectors

is distorted. In the case of the IR detector, the field projected in the sky is rectangular with an aspect ratio of 0.90, which leads to rectangular pixels of 0.135 x 1.121 arcsec. IR spatial area is of 1014 $\times$ 1014 $pixels^2$, so the field of view on the sky is 136 $\times$ 123 arcsec, or 4.65 $arcmin^2$.

In the case of the UVIS detector, the area projected onto the sky has a rhombus shape with an angle between the x-axis and y-axis of 86.1º. This implies that the pixels appear as rhomboids in the sky, measuring an average pixel size of 0.04 arcsec per side. The field of view with WFC3/UVIS is of 162 x 162 $arcsec^2$. UVIS and IR detectors have plate scales of $\sim 0.04 \frac{arcsec}{pixel}$ and $0.13 \frac{arcsec}{pixel}$, respectively.

The instrument ACS (Advanced Camera for Surveys) with WFC (Wide Field Channel) detector has a plate scale of $0.05 \frac{arcsec}{pixel}$ and a field of view of 202 $\times$ 202 $arcsec^2$. This configuration is also subject to geometric distortion.

These distortion effects are purely geometrical and are corrected in the instrument data reduction pipeline.

2.2.2 SExtractor

SExtractor (Source-Extractor) is a software that creates a catalog of objects from an astronomical image. It is specially oriented towards reducing large-scale galaxy survey data; however, it can perform reasonably well on moderately crowded star fields. The analysis of an astronomical image consists of 6 steps: estimation of the sky background by the creation of a "background map", thresholding to detect objects, deblending merged objects, filtering the detections, photometry to obtain isophotal, aperture, and "total" magnitude of an object, and star/galaxy separation, fundamental for extragalactic researches (Bertin & Arnouts (1996)).

SExtractor was used to create a catalog of the galaxies in both clusters (RXJ1347 and RCS0327). The catalogs contain "total light" magnitudes (Kron-like) and also magnitudes from aperture photometry. For this last, we used circular targets centered in the brightest pixel of each galaxy and a diameter of ~0.6″. As Sextractor saved the aperture photometry values in function of the radius of each object in pixel units; we had to convert the galaxy diameter from angular diameter to pixel diameter according to the detector used in each observation (see Table 2.1, Table 2.2 and Section 2.2.1). To realize this task, we had to consider the detector plate scale of each image; in the case of images taken in redder bands `IR` detector was used, which has a plate scale of $0.13\frac{''}{pixel}$, so the diameter was ~5 pixels. In the case of UVIS1 (plate scale of $0.04\frac{''}{pixel}$), the 0.6″ diameter corresponds to 15 pixels. For WFC detector, the plate scale is $0.05\frac{''}{pixel}$, so a diameter of 0.6″ corresponds to 12 pixels.

For both clusters, we used the image in the filter F814W as a detection image. These images were given as input to the `SExtractor` software (Bertin & Arnouts (1996)), which were used as detection images in dual mode to measure the photometry over each HST band, as the images in the different filters are aligned for each cluster.

To estimate the background, we used the parameters `BACK_SIZE`= 256 (mesh size), and `BACK_FILTERSIZE`= 3 (size of the median filter), which we found was a good compromise between the random noise, the presence of objects and the small variations of the background. To correct the background for each detection and the aperture photometry measurements, we set `BACKPHOTO_TYPE` to `LOCAL`. The detection threshold above the local sky background was set to `DETECT_THRESH`= 6.

2.3 MUSE Data

Spectroscopic data was taken by ESO VLT U4, and the instrument used was MUSE. MUSE or Multi-Unit Spectroscopic Explorer is an integral-field spectrograph used to obtain astronomical data in the visible wavelength range. MUSE has been operating at Cerro Paranal in Chile since 2014. It has two operating modes: Wide Field Mode (WFM), where the field of view is of 1x1 $arcmin^2$, and 7.5x7.5 $arcsec^2$ for the Narrow Field Mode (NFM). WFM is the mode used in the observation of both clusters. In this mode, the spatial resolution (FWHM) is 0.3-0.4 arcsec. To boost the spatial resolution, MUSE can use Adaptive Optics (AO), which provides ground-based instruments to overcome the limitation of atmospheric turbulence. In the case of RXJ1347 data, AO was used, not so in the case of RCS0327.

RCS0327 spectroscopic data was taken on 2016-10-01. The cluster was observed around 701 s, and the instrument mode operating was WFM-NOAO-E without AO. The data cube (i.e the final product of the observation) has dimensions of 352 x 329 x 3802 pixels. These dimensions correspond to (x,y,z) where (x,y) are the spatial dimensions and z is the spectral dimension.

In the case of RXJ1347, the target was observed on 2018-03-13 with an exposure time of 8142 s. The cube has dimensions of 704 x 677 x 3681 pixels and, the instrument mode used was WFM-AO-N (with AO). This cube is larger (i.e. contains more spaxels) than RCS0327 because the RXJ1347 cube is the result of the merge of 26 cubes, therefore is a mosaic.

2.3.1 MUSE Field-of-view

MUSE Wide Field Mode (WFM) cover a square field of 1 $arcmin^2$ and the pixel scale corresponds to 0.2 $\frac{''}{pixel}$.

RCS0327 cube has spatial dimensions of 352 x 349 pixels. Considering the pixel scale in the WFM, the size of the sky covered by the observation is 70″ x 70″. Since the cluster is at z= 0.565, the scale is of 6.541 $\frac{kpc}{''}$, which gives a resulting physical size for the cube of 468 x 468 kpc.

On the other hand, RXJ1347 is at z= 0.451. Considering the respectively cube size (704x677 pixel ↔ 140″ x 135″) and the scale at this redshift that is of 5.818 $\frac{kpc}{''}$, we ended up with a cube with physical size of 810 x 785 kpc (spatial dimensions).

2.3.2 PyMUSE

PyMUSE is a Python package to VLT/MUSE. It allows extracting the spectrum from a cube in a specific region shape, combining the spaxels inside an aperture in different ways (Pessa et al. (2018)).

We made use of PyMUSE to extract the spectrum of the regions from the HST catalogs created previously (see Section 2.2.2). This implies that PyMUSE got as input all the parameters that represented every elliptical region: the coordinates of the center (X_0,Y_0), the semi-minor and semi-major axis, and the rotation angle.

The extraction mode utilized was *wwm*, White Weighted Mean; meaning that the spaxels inside a specific aperture are smoothed using a gaussian filter, where the weights are obtained from the white image of the cube.

This package allows us to extract stacked MUSE spectra, for the galaxies identified by SExtractor on the HST images.

2.3.3 Selection of Galaxies

As we said before, for this research, we want to analyze early-type galaxies. We used two manual filters to select the final sample of galaxies for each cluster.

As we know, SExtractor extracts the photometry of the majority of bright objects in an image. This means that other objects can be in the same line of sight of the cluster, for example, stars or spiral galaxies. In this sense, because we used the coordinates of objects classified as galaxies by SExtractor as input to extract the spectra in the MUSE cubes, we need to assess the characteristic of the constituents of the samples, for both clusters.

We based our selection both on photometric and spectroscopic criteria. We analyzed by eye the spectrum of every object extracted with PyMUSE. We discarded the spectrum/objects that did not have the typical features of an elliptical galaxy (Fig. 1.3) and also the spectra that had a low signal-to-noise ratio, that was hard to discern its nature. This filtering reduced the original sample (that contained all the objects from the SExtractor catalogs) considerably. In the second filter, we rectified that the resulting spectra from step one were early-type galaxies. We did such a task by matching every spectrum to the corresponding aperture in the HST F814W image, paying attention to possible spiral structures. This was also done by eye. Third, as we link every spectrum to their respective aperture in the HST images, we ensured that we did not miss any possible elliptical target during steps one and two.

The final sample is formed by 54 early-type galaxies for RXJ1347 cluster and 30 galaxies in the case of RCS0327.

2.3.4 Defining two regions for each Galaxy.

We also analyzed the galaxies in terms of gradients. To aim this purpose, we extracted the spectrum of two regions for each galaxy: a central circular region and an outer annular region, both regions containing the same amount of light (~50%). In order to define both regions, we used the white image of each cube and the ellipse parameters from the SExtractor catalog, as well as we did in Section 2.3.3 to extract the spectrum of each galaxy. The only difference in this instance was that we worked with circular apertures instead of elliptical, using $R_{semi-major-axis} = R_{gal}$. In this way, every galaxy is described as a circular region containing "all" the light of the galaxy. The outer radius (R_{gal}) is the one enclosing the total light from the galaxy in the MUSE image.

We needed to separate the circular apertures of each galaxy into two regions, a central circular region, and an annulus, both containing equal light. The inner radius was automatically retrieved by splitting the total MUSE light (which came from the aperture with radius R_{gal}) in a half. This was done numerically. Using this approach, we split each galaxy into a central circular region of radius r and an outer annulus with an internal radius of r and external radius R_{gal}.

The outer radius is the one enclosing the total light from the galaxy in the MUSE image

Chapter 3

Spectral Analysis

Now that we have our final sample of galaxies, we want to study the properties of their stellar populations. As commented in Section 1.1.2 a galaxy is conformed by stars with different ages, metallicity, surface temperature, etc. Thus a spectrum is the light contribution of all-stars inside a galaxy. To analyze the properties of a spectrum, we used pPXF.

Penalized Pixel-Fitting is a method to fit the stellar population of galaxies and the stellar and gas kinematics. Complete information about the method can be found in Cappellari & Emsellem (2004) and Cappellari (2017), here we reviewed these two papers.

3.1 pPXF: Penalized Pixel-Fitting Method

The pPXF method aims to recover a parametric Line-of-Sight Velocity Distribution (LOSVD) from absorption-line spectra of galaxies through Penalized Likelihood (Cappellari & Emsellem (2004)). To recover the LOSDV, we need to know the LOSVD at all spatial positions on a galaxy image. To recover the LOSVD from the observations, we have to consider galaxies as perfect stellar systems, so if we point at a specific position of the sky, the spectrum observed will be a light-weighted sum of specific stellar spectra

redshifted depending on their Line-of-Sight (LOS) velocities.

Let's suppose that the spectrum of a galaxy (light from all its stars) is given by a single template. In this case, the problem of recovering the LOSVD from the data comes from the convolution between that spectrum and the LOSVD (which is what we are looking for). This can be solved by solving the inverse problem, i.e. deconvolving the spectrum using the template.

This technique has some advantages as it can be performed directly in the pixel space, so excluding gas emissions lines or bad pixels from the fit is simple. Another benefit comes from the computational cost involved and the current technology, making it easier to run this type of code on personal laptops. Besides, the availability of libraries with high spectral resolution enables a good match between the templates and the observed spectrum.

The parametric recovery of the LOSVD in pixel space begins with creating a model galaxy spectrum $G_{mod}(\mathrm{x})$, by convolving a template spectrum $T(\mathrm{x})$ by a parametrized LOSVD. The object (observed spectrum) and the spectra from the templates are rebbinned in wavelength to a linear scale $x = ln(\lambda)$, preserving the number of spectral pixels. $x = ln(\lambda)$ ensures a constant velocity scale for every x. This implies that the LOSVD remains constant along the x coordinate, allowing efficient use of the Fast Fourier Transform (FFT) methods when performing the convolution (Cappellari (2017)).

The best-fitting parameters of the LOSVD come from minimizing the measure of agreement between the model and the observed galaxy spectrum $G(x)$; this corresponds to minimize χ^2, defined as Equation 3.1:

$$\chi^2 = \sum_{n=1}^{N} r_n^2 \tag{3.1}$$

where residuals (r_n) are defined as

$$r_n = \frac{G_{mod}(X_n) - G(X_n)}{\Delta G(X_n)} \tag{3.2}$$

$\Delta G(X_n)$ is measurement error on $G(X_n)$.

Thus the model adopted for the galaxy spectrum is described by Equation 3.3:

$$G_{mod}(x) = \sum_{k=1}^{K} w_k [B * T_k](x) + \sum_{l=0}^{L} b_l P_l(x) \tag{3.3}$$

T_k is a library of K galaxies or stellar templates.

$B(x) = \mathcal{L}(cx)$ is the broadening function.

c is the speed of light.

$\mathcal{L}(v)$ is the LOSVD.

$P_l(x)$: legendre polynomials of order l.

* denotes convolution.

For every given $\mathcal{L}$(v) (LOSVD), we have to optimize χ^2 what is a bounded- variable linear least-square problem for the weights (w_1, ..., w_K, b_0,..., b_L). The point is to determinate the parameters for $\mathcal{L}$(v), assuming the weight are already optimized. We expand the LOSVD as a Gauss-Hermite series, Equation 3.4:

$$\mathcal{L}(v) = \frac{e^{-(1/2)y^2}}{\sigma\sqrt{2\pi}} \left(1 + \sum_{m=3}^{M} h_m H_m(y)\right) \tag{3.4}$$

where

$y = \frac{v - V}{\sigma}$ and H_m are the Hermite polynomials.

Minimizing χ^2 of Equation 3.1 is a problem of non linear least square optimization for the M parameter (V, σ, h_3, ..., h_M), this can be sort out with a algorithm in which the residuals r_n (Equation 3.2) are provide by the user, thereby it is possible to compute explicitly the Hessian matrix of the χ^2.

However, there is a different approach to the determination of the best-fitting parameters of the LOSVD in Equation 3.4, this is the **Penalized Pixel Fitting method**, which fits all parameters simultaneously.

The LOSVD of galaxies is, in general, similar to a Gaussian. In Penalized Pixel Fitting method, they apply the formalism to the case in which the LOSVD is parametrically expanded as a Gauss-Hermite series. The concept is to fit the parameters (V, σ, h_3, ..., h_M) simultaneously, adding an adjustable penalty term to the higher χ^2 to bias the solution towards a Gaussian, when the data unconstrain the higher moments. Thus we have a penalized χ^2 (Equation 3.5):

$$\chi_p^2 = \chi^2 + \alpha P \tag{3.5}$$

where P is the penalty function and α is the penalty factor.

P is given by the integrated square deviation of $\mathcal{L}(v)$ from its best-fitting Gaussian $G(v)$:

$$D^2 = \frac{\int_{-\infty}^{\infty} [\mathcal{L}(v) - G(v)]^2 dv}{\int_{-\infty}^{\infty} G(v)^2 dv} \tag{3.6}$$

When $\mathcal{L}(v)$ is described by Equation 3.4, Equation 3.6 can be approximated by:

$$D^2 \approx \sum_{m=3}^{M} h_m^2 \tag{3.7}$$

It is not advisable optimize χ_p^2 defining $P = D^2$ for mainly two reasons: it is more efficient to minimize the residuals r_n from Equation 3.2 that compute χ_p^2 in terms of computational time. Also, if $P = D^2$ is necessary to adjust the penalty factor α according to the χ^2 of the observed fit.

A solution to these issues is to use perturbed residuals as input to the nonlinear least-square optimizer:

$$r'_n = r_n + \lambda\sigma(\vec{r})D \tag{3.8}$$

where the variance is

$$\sigma^2(\vec{r}) = \frac{1}{N} + \sum_{n=1}^{N} r_n^2 \tag{3.9}$$

D can be interpreted as a deviation of the LOSVD from a Gaussian shape. This deviation will be accepted as a refinement of the fit only if the scatter $\sigma(\vec{r})$ decreases. The objective function of the fit in consequence is:

$$\chi_p^2 = \sum_{n=1}^{N} r_n^2 + 2\lambda\sigma(\vec{r})D\sum_{n=1}^{N} r_n + N[\lambda\sigma(\vec{r})D]^2 \tag{3.10}$$

$(\sum_{n=1}^{N} r_n)$ is equal to zero by construction, since the weights are optimized for a given $\mathcal{L}(v)$. Considering Equation 3.9, Equation 3.10 becomes:

$$\chi_p^2 = \chi^2(1 + \lambda^2 D^2) \tag{3.11}$$

Equation 3.13 is the final form of Equation 3.5 where $\alpha = \lambda^2 D^2$ is naturally scaled according to the χ^2 of the fit.

Different forms of Equation 3.8 are admissible, with the requisite that the objective function has the form of Equation 3.5. One form is to add multiplicative perturbation of the residual:

$$r'_n = r_n(1 + \sigma D^2) \tag{3.12}$$

so the resulting objective function is:

$$\chi^2_p = \chi^2(1 + 2\lambda D^2 + \lambda^2 D^4) \tag{3.13}$$

If we ignored the term D^4 (too small) the results is similar to Equation 3.5, where $\alpha = 2\lambda\chi^2$.

An updated version of pPXF in which the method was review and improved was published in 2017 (Cappellari (2017)). Thereby the updated version of Equation 3.3 (i.e. the expression of the observed galaxy spectrum using the parametrization) is given by:

$$G_{mod}(x) = \sum_{n=1}^{N} w_n\{[T_n(x) * \mathcal{L}_n(cx)] \sum_{k=1}^{K} a_k P_k(x)\} + \sum_{l=0}^{L} b_l P_l + \sum_{j=0}^{J} c_j S_j \tag{3.14}$$

Where $\mathcal{L}_n$ is the LOSVD that can be different for the N templates T_n. S_j are the spectra of the sky.

The method adds multiplicative polynomials (P_k) to make the fit insensitive to extinction by dust avoiding a reddening curve as input and also corrects inexactness in the spectral calibration. It also aggregates additive polynomials (P_l) to minimize template mismatch by modifying the strength of individual absorption lines and to precise imperfect sky subtraction or scattered light. Both multiplicative and additive polynomials can be Legendre type or a truncated Fourier series, of degree k and l.

In summary, the algorithm of the Penalized Pixel Fitting to recover the LOSVD parametrized as a Gauss-Hermite series is:

1. Begin with the initial guess to (V, σ), and the Gauss-Hermite parameters set to zero (h_3,..., h_M= 0).
2. Solve Equation 3.3 for the weights (w_1,..., w_K, b_0,..., b_L).
3. Calculate the residuals r_n from the fit, through Equation 3.2.
4. Get r'_n perturbing the residuals from Equation 3.8.
5. Introduce r'_n (perturbed residuals) into a non linear least-square optimization program and repeat the series of steps from 2) to fit the parameters (V, σ, h_3,..., h_M).

A representative pPXF fit is presented in Fig. 3.1.

3.2 Templates: MILES

Templates can consist of combinations of (Cappellari (2017)):

1. Stellar population models with specific parameters.
2. Individual empirical or synthetic stars.
3. Principal components derived from a library of spectra.

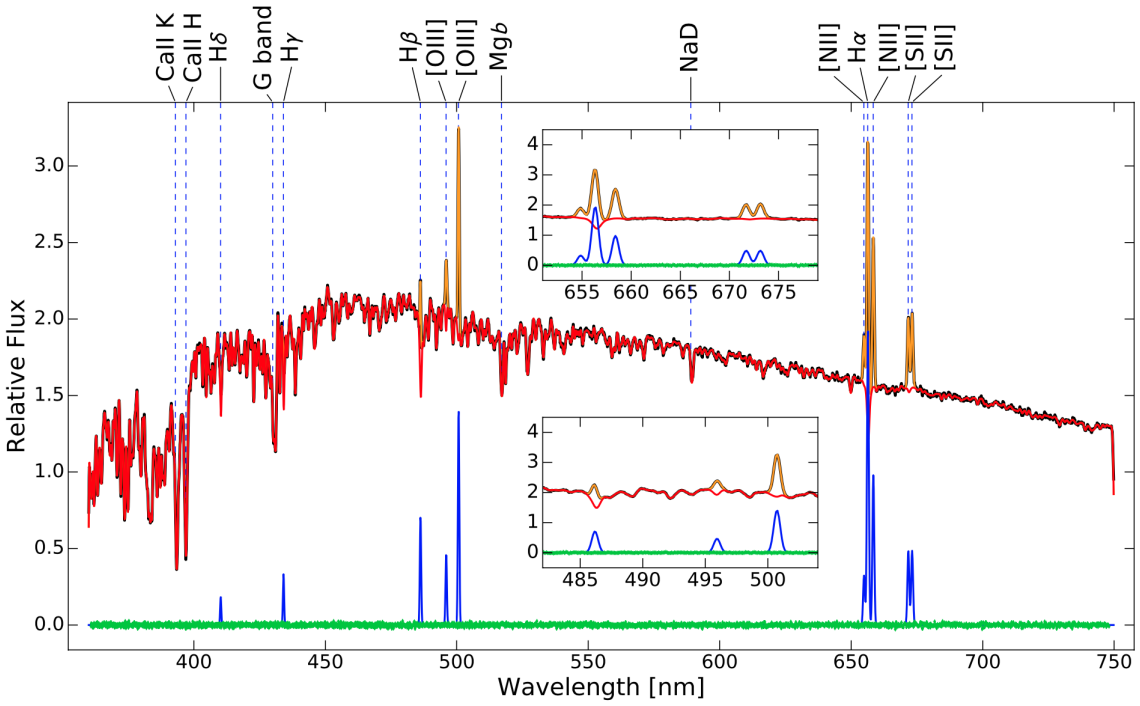

Figure 3.1: Representative pPXF fit to the solar spectrum and to the added emission lines. The hidden black line is the relative flux of the observed spectrum. The red line is the pPXF fit to the stellar component. The orange line is a fit for the gas emission lines. The green line at the bottom part of the plot is the fit residuals, while the blue line is the gas-only best-fitting spectrum. The primary absorption and emission components are indicated in the upper part of the plot. Subplots show a zoomed view of the pPXF fits and residuals in the regions, including the $H\alpha$ (top) and $H\beta$ (bottom) lines. Image from Cappellari (2017).

4. Weighted sum of different stars.

5. Gas emission lines.

6. Sky spectra.

Stellar population models with specific parameters '1)' are used in pPXF "full-spectrum" fitting modality. As we explained before, this method is helpful to investigate the stellar populations of galaxies. Besides, it is helpful to extract the stellar and gas kinematics. In this context, we need templates to compare observation with them.

MILES (Medium-resolution Isaac Newton Telescope Library of Empirical spectra) library consists of 958 stars covering from 3525Å to 7500Å with spectral resolution of 2.5Å at FWHM (full-width half-maximum) (Beifiori et al. (2011)). This stellar library was used for the creation of empirical models for stellar population synthesis Vazdekis et al. (2010b). The spectra were observed with the 2.5-m Isaac Newton Telescope in Spain during 2000 and 2001. To guarantee homogeneity, all the spectra were observed with the same instrumental configuration.

The sample (Sánchez-Blázquez et al. (2006)) was selected trying to reduce peculiar stars, spectroscopic binaries, stars that present chromospheric emission, and stars with high variability in zones of the HR diagram where variability is significant. In this way, the sample is composed mostly of field stars from the solar neighborhood, covering a broad range in age (from open clusters) and different metallicities (from Galactic globular clusters) (see Fig. 3.2). The sample also contains G8-K0 metal-rich stars ($+0.02 <$ [Fe/H]$< +0.5$), with temperatures ranging between 5200-5500 K. Additionally, stars with T$>$ 6000 K and metallicity higher than +0.2 were added to decrease uncertainties in the prediction of the model around this metallicity. Also, to predict the turn-off of the main sequence, they include hot dwarf since their high contribution to the total light. The sample also has dwarf stars with T$<$ 5000 K to make predictions using initial mass functions (IMF) with high slopes. They also added 17 cool and metal-rich giant

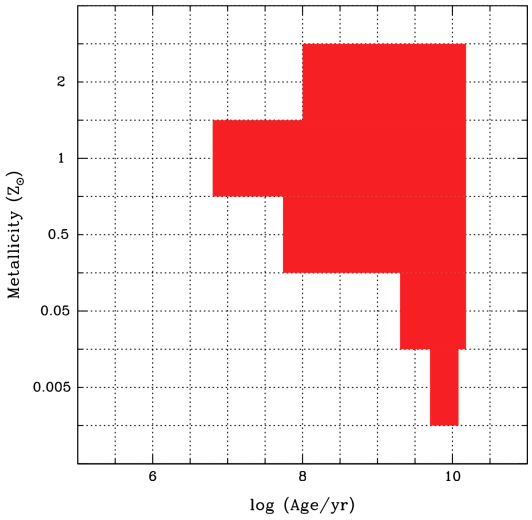

Figure 3.2: Age and metallicity coverage of MILES library. Image from Maraston & Strömbäck (2011).

stars ([Fe/H]$> +0.15$). Finally, to study the consequences of the horizontal branch and enhance predictions for old stellar populations, they included metal-poor giant stars with $T_{eff} <$ 6000 K.

We used in this work an extended version of MILES templates, *E-MILES*. *E-MILES* stellar populations models cover the spectral range from 1680 to 50000Å. The models span the metallicity range -1.79 $< [M/H] <$ +0.26 and ages between $1-17.8$ Gyr (see more: E-MILES).

3.2.1 Stellar population synthesis model predictions using MILES stellar library

Evolutionary population synthesis models consider the contributions of all possible stars in proportions prescribed by stellar evolution theory. The models combine at least three main ingredients that determine the quality of the predictions: a prescription for the IMF (Initial-mass-function), a set of stellar evolutionary isochrones in several bands,

such as fluxes, colors, M/L or low-resolution spectra, and surface brightness fluctuations (Vazdekis et al. (2010a)).

The initial mass function (IMF) is an empirical function that describes the mass distribution of a newly formed population of stars. Thus the IMF is the result of a star formation process. MILES models, which we used in this work, adopt IMF shapes described in (Vazdekis et al. (1996)), Unimodal IMF, is represented by a power-law function characterized by its slope as a free parameter. Salpeter determined the IMF for stars in the Solar neighborhood in 1955. The standard Salpeter IMF (Salpeter (1955)) is obtained when the slope value is 1.3, and this value for the slope was used to compute our results.

When we want to infer ages from integrated spectra, different definitions of age can be used as (Gonçalves et al. (2020)):

- Isochrones age (t_{iso}): this is the age inferred from isochrone fitting, obtained from fitting stellar evolution isochrones to observed color-magnitude diagrams.
- Light-weighted age (t_{light}): this is obtained by a multi-population mean age, computed by weighting the age of each simple stellar population element (SSP_j) by its light contribution (x_j), giving as results

$$\langle log(age) \rangle = \sum_j x_j \log(age)_j \tag{3.15}$$

- Mass-weighted age (t_{mass}): analogous to t_{light} but the age of each simple stellar population element (SSP_j) is weighted by its stellar mass.
- SSP-equivalent age (t_{SSP}): age of the SSP that best fits the observation (SSP model with the smallest χ^2).
- Age of the top contributor to the total light (t_{max,x_j}): is the age of the SSP which most contributes to the integrated light ($max(x_j)$).

In the case of our research, we work with light-weighted ages.

One of the theoretical isochrones sets of the SSP models used by MILES library is PADOVA+00, which is the one that we used in our research. (Girardi et al. (2000)).

The scaled-solar isochrones or PADOVA+00 are presented by a large grid of stellar evolutionary tracks, which are suitable to modeling star clusters and galaxies by means of population synthesis. The tracks are arranged for the initial chemical compositions [Z = 0.0004, Y = 0.23], [Z = 0.001, Y = 0.23], [Z = 0.004, Y = 0.24], [Z = 0.008, Y = 0.25], [Z = 0.019, Y = 0.273] (solar composition), and [Z = 0.03, Y = 0.30], this means that the isochrones cover six metallicity bins (Z = 0.0004, 0.001, 0.004, 0.008, 0.019 and 0.03), where Z = 0.019 corresponds to the solar metallicity.

These tracks are computed taking into account opacities, equation of state, and a moderate convective overshoot. The range of initial stellar masses extends from $0.157M_{\odot}$ to $7M_{\odot}$, and the evolutionary phases go from the zero-age main sequence or ZAMS to later stages of stellar evolution, either the thermally pulsing AGB regime or carbon ignition. As we know, most of the evolutionary tracks follow a linear $Y(Z)$ relation of the form $Y = Y_p + (\Delta Y/\Delta Z)Z$. Girardi et al. (2000) adopted values of Y_p =0.23 and $(\Delta Y/\Delta Z) = 2.25$. This means that the helium fraction adopted follows the relation: $Y = 0.23 + 2.25Z$.

Padova isochrones cover a broad range of ages, from 0.063 to 17.8 Gyr. The input physics and coverage of the Z-Y plane of these models were updated with improved versions of the equation of state, the opacities, reaction rates, and convective overshoot scheme.

3.3 pPXF Setting

We used pPXF to fit our spectra between 3000Å - 7000Å. We used all the available *E-MILES* templates without cutting them by age. The number of kinematic moments fitted was 2. The degree of the additive and multiplicative Legendre polynomial was 8 and 10, respectively. We set $N_{sim} = 512$, with N_{sim} being the number of Monte-Carlo simulations used to extract errors on the stellar kinematics.

We fitted all spectra with two values of regularization, REGUL = 0 and REGUL = 30. So for each galaxy we got unregularized and regularized stellar population parameters.

3.3.1 Regularization Parameter

In pPXF, the regularization can be set by a unique parameter, the regularization parameter. It is desired that the current-χ^2 (χ^2_{curr}) can be as close as possible to the desired-χ^2 (χ^2_{des}), but not higher. The regularization is a measurement of the smoothness of weights of the templates with similar metallicity and ages; at the higher regularization parameter, the solution is more smooth.

In order to set a reasonable regularization, first we measure the unregularized χ^2 ('regul'=0, keyword in PPXF). Then, N_{DOF}, the degree of freedom or number of unmasked pixels in the input spectrum, was increased until $\chi^2/N_{DOF} = 1$. The fit to every spectrum can be computed again with an increment of the 'regul' until the χ^2_{des} value is such that $\Delta\chi^2 = \sqrt{2N_{DOF}}$. This criterion helps to get a fit that represents the star-formation history of the galaxy and that also reflects the original spectrum. However, $\Delta\chi^2 = \sqrt{2N_{DOF}}$ is not always possible to find without setting a huge regularization, so we used Shetty & Cappellari (2015) approach for χ^2_{des} that requires $\Delta\chi^2 = \sqrt{2N_{DOF}}/6$, as a lower limit for χ^2_{des}. This limit works well for low-S/N spectra and does not dramatically affect the values for high-S/N spectra.

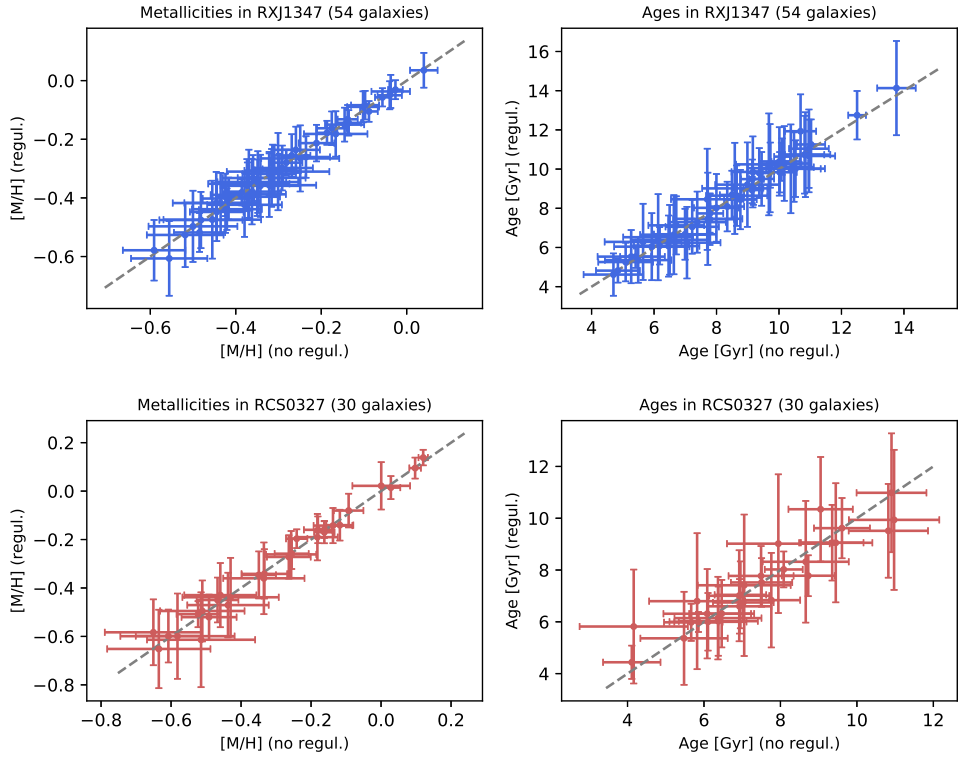

Figure 3.3: Comparison between stellar population parameters obtained from regularized ('regul'= 30) and non-regularized pPXF fits. Grey dashed lines indicate one-to-one relations. Errors comes from Monte Carlo simulation with 512 simulations per galaxy.

In our work, we used a regularization of REGUL= 30 for each galaxy spectrum. We compared the light-weighted stellar population parameters computed from regularized and non-regularized PPXF fits. In Fig. 3.3 is possible to see a good agreement between the regularized and unregularized fits, showing that results are not significantly affected by the regularization used.

3.3.2 Error Estimation

We infer the uncertainties of each parameter calculated using a Monte Carlo approach to bootstrap. We sampled each spectrum 512 times by resampling the pixels

from the best fit model residuals (noise), starting from the noise of the unregularized best fit. We performed 512 simulations per galaxy/spectrum because we found this number is in good agreement with the computational specifications and performing time of the machine that we used, which consisted of 16 cores.

The error estimation depends on the S/N (signal-to-noise) ratio of the spectrum of each galaxy. Bootstrapping also helps us break the age-metallicity degeneracy since, for each galaxy, we obtain a distribution of solutions that can be wide or narrow depending on the S/N ratio.

3.4 Stellar Population Synthesis Model

In 2003, Bruzual & Charlot (2003) presented a stellar population synthesis model for computing the spectral evolution at ages between 0.1 Myr and 20 Gyr at a resolution of 3 Å across a wavelength range from 3200 to 9500 Å for a broad range of metallicities. The model is based on observed spectra, and it as well incorporates stellar evolution theory and an observational prescription for thermally pulsing stars on the asymptotic giant branch (TP-AGB). Also, the model reproduces the observed optical and NIR color-magnitude diagrams of Galactic star clusters of various ages and metallicities adequately. This last was tested using galaxy spectra from the Early Data Release (EDR) of the Sloan Digital Sky Survey (SDSS).

In our work, we used the Charlot & Bruzual (from now on CB09) models, which are formally identical to the Bruzual & Charlot (Bruzual & Charlot (2003) or BC03) models but incorporate significant improvements.

CB09 utilizes the tracks up to 15 $M_{\odot}$ from the previous models with upgraded input physics. CB09 uses the called Padova 1994 tracks for stars with masses in the range of 20-120 $M_{\odot}$. According to an updated semi-empirical prescription, the TP-AGB evolu-

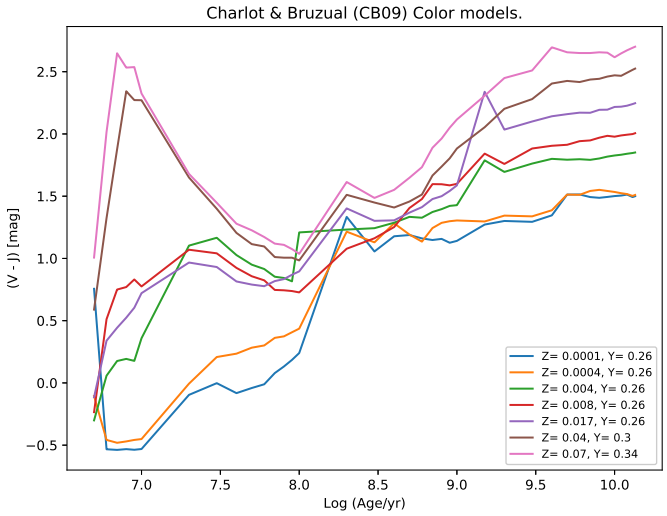

Figure 3.4: Colors of Charlot & Bruzual models (CB09). Z indicates initial metallicity, Y initial helium fraction, and (V - J) is a color computed from the V-band and the J-band as a function of time.

tion of low and intermediate-mass stars is followed, including theoretical improvements over prior calculations. It has also been calibrated with the help of carbon star luminosity functions in the Magellanic Clouds and TP-AGB lifetimes (star counts) in Magellanic Cloud clusters. CB09 tracks account for 15 evolutionary stages in the TP-AGB (six in the O-rich phase, six in the C-rich phase, and three in the superwind phase), while the BC03 models included a unique evolutionary stage at each phase (González-López et al. (2010) and G. Bruzual, 2009).

CB09 color models as a function of time for different initial metallicity and helium fraction can be seen in Fig. 3.4. We used these models to compare colors from our HST photometry data to colors from CB09 models, according ages and metallicities.

3.5 Λ-CDM Cosmology

Throughout all this work we assumed a flat ΛCDM with $\Omega_M = 0.28$, $\Omega_{vac} = 0.714$, and $H_0 = 69.6\ km\,s^{-1}Mpc^{-1}$. With this, is now 13.720 Gyr since the Big Bang.

At z = 0.45 (redshift of RXJ1347), the age since the Big Bang is 9.0 Gyr. This gives a scale of $5.818\frac{kpc}{''}$ (Wright (2006)).

At z = 0.56 (redshift of RCS0327), the age since the Big Bang is 8.2 Gyr. This gives a scale of $6.541\frac{kpc}{''}$ (Wright (2006)).

Chapter 4

Results and discussion

We determined the cosmogical spectroscopic redshifts for the galaxies members of both cluster. If we remember the redshift of the clusters from Section 3.5, we can say that galaxies are distributed in a radius of z ~0.016 centered in $z(RXJ1347)$ =0.451 and $z(RCS0327)$ =0.564. This can be appreciated in Fig. 4.1 and Fig. 4.2. We have identified, respectively, 54 and 30 galaxies as members of the respective clusters.

We computed the stellar population parameters using the $pPXF$ method (see Section 3.1). Fig. 4.3 shows the galaxies ages distribution in RXJ1347 and RCS0327. The mean age for galaxies in RXJ1347 is ~ 8.6±2.1 Gyr. In RCS0327, the mean age of the galaxies is ~ 7.5±1.6 Gyr. It is important to consider that the physical size of RXJ1347 is ~ 1.8 times bigger than the FoV of RCS0327. This can explain the difference between the number of galaxies members in the final sample of each cluster.

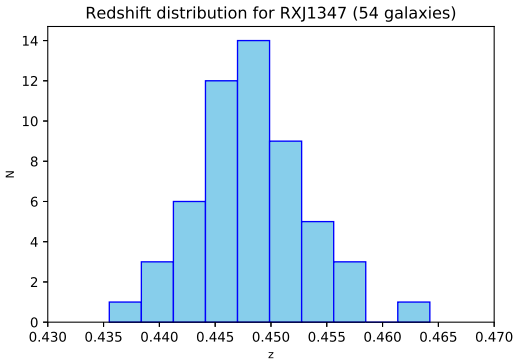

Figure 4.1: Redshift distribution for galaxies in RXJ1347.

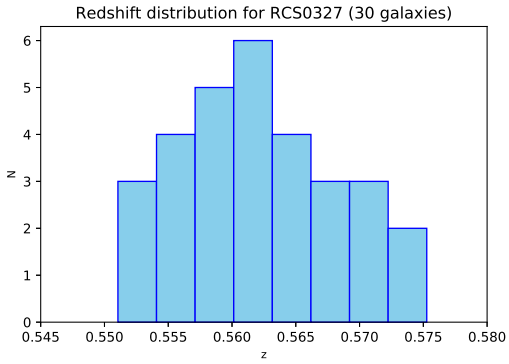

Figure 4.2: Redshift distribution for galaxies in RCS0327.

If we consider the same physical size (in kpc) for both clusters, the statistical values for ages in RXJ1347 do not change significantly, resulting in a mean age for the galaxies of ~8.8±2.3 Gyr. The number of galaxies is then reduced from 54 to 30 galaxies in RXJ1347, so it is viable to say that at the same physical cluster size, both clusters have a similar number of members.

Furthermore, in the case of the total metallicities measurement, the distribution for the metallicity of the galaxies belonging to both clusters are not comparable (see Fig. 4.4). In the case of RXJ1347 is possible to appreciate a clear peak in the distribution, unlike in RCS0327 metallicity distribution. In this last, the metallicity distribution seems almost uniform. However, the mean values for the total metallicity are similar, being [M/H]~ -0.30±0.15 (Z ~ 0.010±0.004) and [M/H]~ -0.31±0.22 (Z ~ 0.013±0.003) for RXJ1347 and RCS0327, respectively. At the same physical FoV, these values do not change drastically. So our sample contains a wide range of metallicities, mostly galaxies have marginally sub-solar metallicities.

Citro et al. (2016) studied the median stacked spectra of a sample of more than 20,000 massive and passive early-type galaxies (ETGs) at $0 < z < 0.3$ from the Sloan Digital Sky Survey (SDSS DR4), finding out that the stellar metallicities are slightly

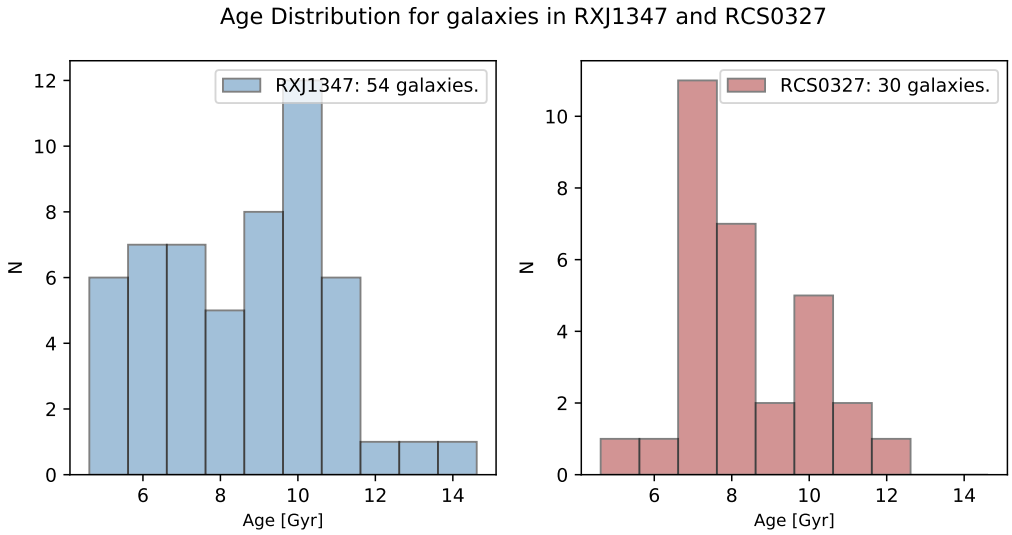

Figure 4.3: Light-weighted ages for galaxies in RXJ1347 and RCS0327 clusters. At z =0.45 the age of the universe is ~9 Gyr and at z =0.56 is ~8.2 Gyr. The age distribution of RCS0327 has been displaced 0.8 Gyr to the right to compare the galaxies of both clusters at the same redshift.

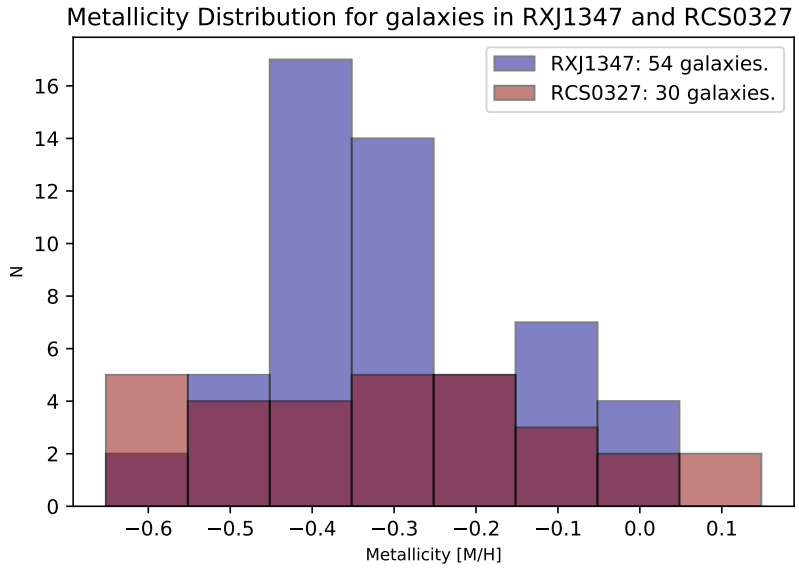

Figure 4.4: Light-weighted total metallicities for galaxies in RXJ1347 and RCS0327.

supersolar, with a mean of Z ~0.027±0.002, depending on the spectral synthesis models used for the fit. Also, they found that the metallicity did not depend on redshift in their sample. Notwithstanding that their metallicities are consistent with other results at a fixed stellar mass, a high scatter is exhibited between the estimates of the metallicity obtained with different methods.

4.1 Brightness, Metallicity and Age

We calculated mean ages and mean metallicities (both parameter are light-weighted) for the sample of galaxies. The error values for each parameter comes from performing Monte Carlo simulations (see Section 3.3.2). For both cluster we see that in general the brightest galaxies are also the more metal-rich, suggesting a brightness-metallicity relation (Fig. 4.5 and Fig. 4.6). For the galaxy photometry in each cluster, we selected two different set of HST bands (F125W-F475W and F160W-F606W), in order to analyze the more similar brightness considering the redshift of the respective cluster. We also can see in the figures previously mentioned that ages are poorly constrained for metal-poor galaxies.

Worthey et al. (1995) suggested the presence of a metallicity-age relation in E/S0 galaxies, where younger galaxies appear more metal-rich than old ones. We do not see this behaviour in our data. In fact, in Fig. 4.7 and Fig. 4.8 we do not see it at all. It is important to consider that we are performing a full-spectrum fitting and that we are not only limitating to fit age-sensitive (e.g. Hβ) or metal-sensitive (e.g. Mg_b, <Fe>) indicators. For this reason, it is reasonable to see a break of the age-metallicity degeneracy in the upper right plot of Fig. 4.7 and Fig. 4.8.

Some studies have shown that the stellar velocity dispersion in quiescent galaxies is related to its dark matter halo, so on to its total mass (at z $<$ 0.7) (Zahid et al.

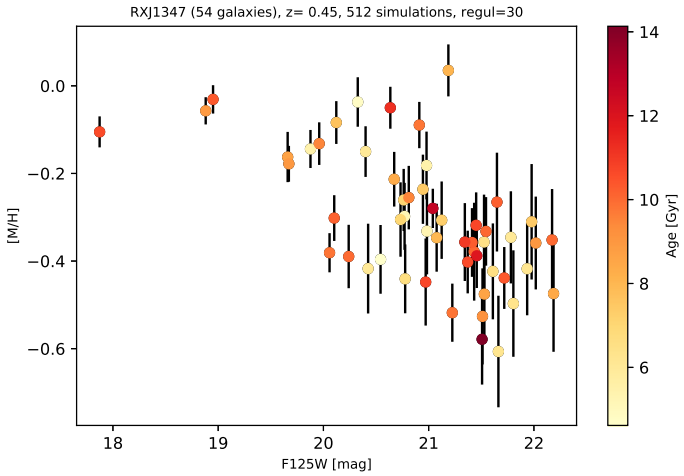

Figure 4.5: Derived galaxy metallicity as a function of galaxy brightness in the F125W for galaxies in RXJ1347. The error bars show the 1σ distribution of metallicity values for each galaxy based on its 512 simulation. Colors for each galaxy correspond to the mean age of their stellar populations.

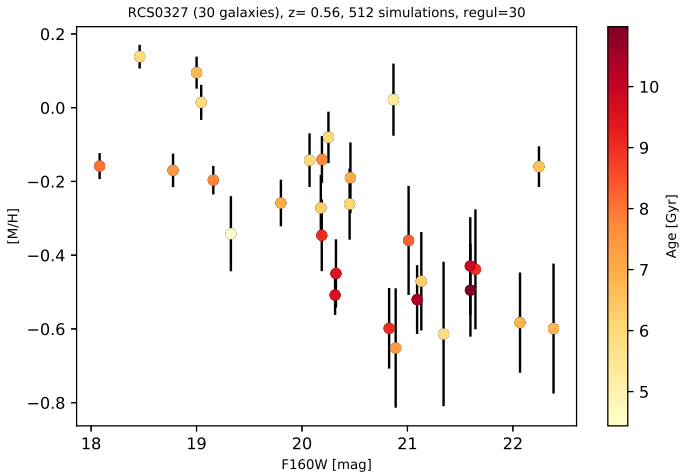

Figure 4.6: Derived galaxy metallicity as a function of galaxy brightness in the F160W HST filter for galaxies in RCS0327. The error bars show the 1σ distribution of metallicity values for each galaxy based on its 512 simulation. Colors for each galaxy correspond to the mean age of their stellar populations.

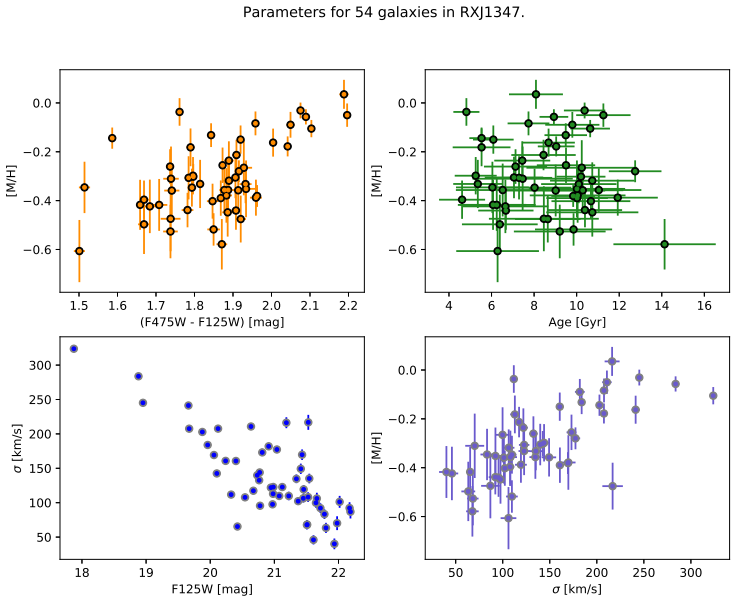

Figure 4.7: Apparent magnitude in F125W and F475W bands, age, color, and velocity dispersion for members of RXJ1347. The error bars show the 1σ distribution of the respective values for each galaxy based on its 512 simulations for parameters retrieved with $pPXF$ and are light-weighted.

(2016)). This also has been tested with hydrodynamical simulations, which suggest that quiescent galaxies are in virial equilibrium (Zahid et al. (2018)). We also observed in both clusters (Fig. 4.7 and Fig. 4.8) that the more luminous galaxies have a higher velocity dispersion, and also that they tend to have higher metallicities. The luminosity of a galaxy is related to its mass (see Section 1.1.1). Thus, it is viable to say that more massive galaxies are more luminous and have higher stellar velocity dispersion. From the figures mentioned in this section, it is difficult to establish a clear relation between metallicity/luminosity/σ and the stellar age of the galaxy population.

4.2 Color-magnitude diagrams

We show F125W - F475W and F160W - F606W color-magnitude diagrams (CMDs) for the two clusters, RXJ1347, and RCS0327, in Fig. 4.9 and Fig. 4.10, respectively.

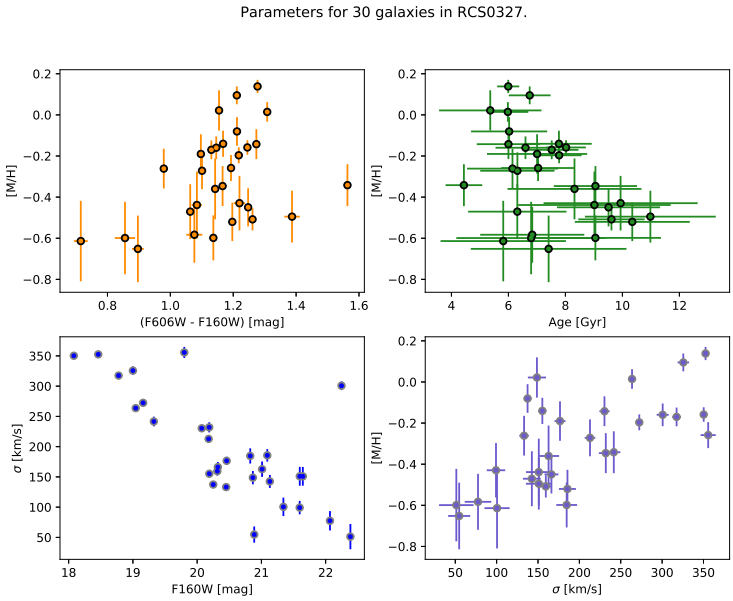

Figure 4.8: Apparent magnitude in F160W and F606W filters, age, color, and velocity dispersion for members of RCS0327. The error bars show the 1σ distribution of the respective values for each galaxy based on its 512 simulations for parameters retrieved with $pPXF$ and are light-weighted.

Blue and red circles show cluster galaxies with and without spectroscopic redshifts. We chose both sets of filters according to the redshift of the clusters. Thereby we can compare both clusters at a similar "rest-frame color".

Our fit for the red sequence is shown with the green line in the CMDs. The fit was computed using all the MUSE galaxies (blue circles). To determine which galaxies were cluster members of the red sequence, we simulated a gaussian population of 1000 galaxies and computed their (V-J) colors; these filters were the nearest to our HST bands used (see Section 4.3).

We defined the limits of the red sequence using the simulated population considering the 1σ of the galaxy's simulated colors. These limits can be seen in Fig. 4.9 and Fig. 4.10 represented by orange lines. In this way, blue dots within these limits are

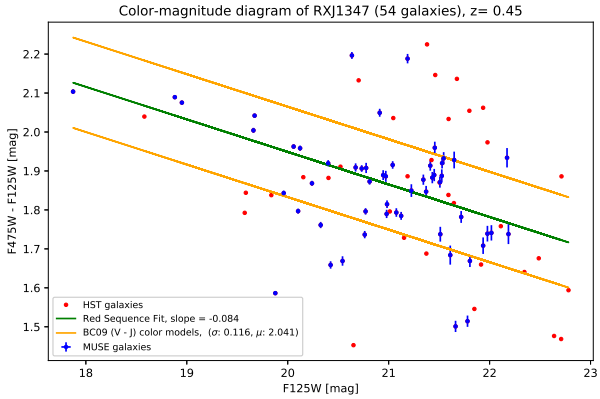

Figure 4.9: Color-magnitude diagram for RXJ1347.Blue dots correspond to galaxies in the MUSE field-of-view for which we have spectroscopic and photometric data. Red dots correspond to galaxies in the HST FOV that only have photometry data. The green line is our fit to the Red Sequence of the cluster, which we did it using galaxies in the MUSE field-of-view. Orange lines delimit the 1σ of a simulated population.

cluster members of the red sequence.

For RXJ1347 of the total 54 galaxies, only 38 belong to the red sequence. In the case of RCS0327, 24 of 30 members are red sequence galaxies.

The differences in relative ages between the galaxies members of the same cluster can be linked to the timescale formation of each of them. Some studies have reported an age difference between red sequence early-type galaxies in clusters and low-density regions from $\sim$ 1.2 Gyr (Bernardi et al. (1998)) up to 2 - 3 Gyr (Kuntschner et al. (2002)). Conroy et al. (2013), studied early-type galaxies at $0.025 < z < 0.06$ and found a distribution of light-weighted ages ranging from 6 - 12 Gyr. Connor et al. (2019) also present red sequence early-type galaxies at $z = 0.35$ with ages ranging from 3 to 8 Gyr. In our case, the ages standard deviation for red sequence galaxies in RXJ1347 is $\sim$ 2 Gyr and RCS0327 $\sim$ 1.4 Gyr, ranging from $\sim$ 5 Gyr to $\sim$ 13 Gyr.

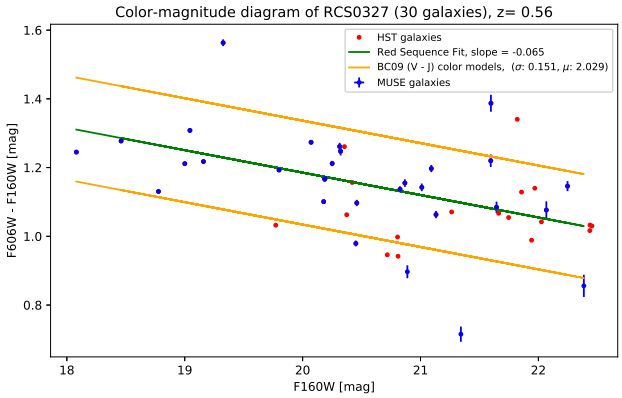

Figure 4.10: Color-magnitude diagram for RCS0327. Blue dots correspond to galaxies in the MUSE field-of-view for which we have spectroscopic and photometric data. Red dots correspond to galaxies in the HST FOV that only have photometry data. The green line is our fit to the Red Sequence of the cluster, which we did it using galaxies in the MUSE field-of-view. Orange lines delimit the 1σ of a simulated population.

4.3 Simulated Populations of Galaxies

As we mentioned in Section 4.2, we computed a simulated population for the two clusters. This was done with the aim of establishing a comparison between our data and the color models available.

First, we used the mean and the standard deviation of the ages and metallicities of the galaxies of both clusters. With these values, we simulated a normally distributed population of 1000 galaxies in both cases. So, as a result, we obtained 1000 galaxies having a determined age and metallicity following Gaussian distributions with parameters given by the actual measurements.

Lastly, we used Bruzual & Charlot color models (see Section 3.4) to link the corresponding color in the (V - J) filters for each of the 1000 galaxies, following their respective simulated age and metallicity.

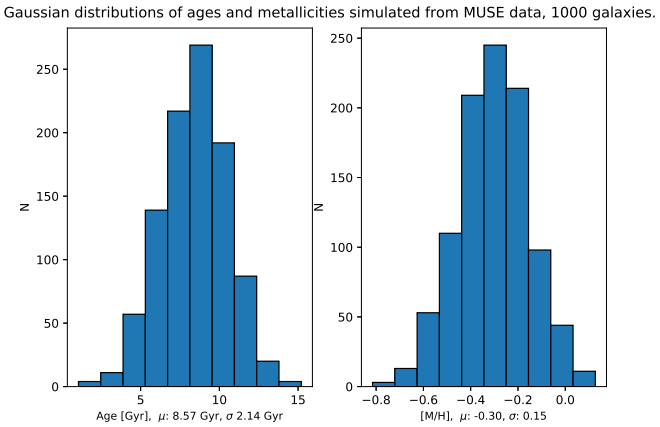

Figure 4.11: Normal distributions for age and metallicity using the mean and the standard deviation of ages and metallicity calculated with pPXF. The simulated population consisted in 1000 galaxies for RXJ1347.

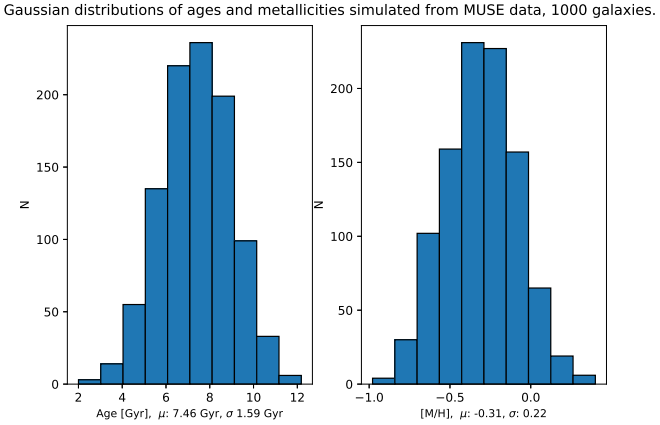

Figure 4.12: Normal distributions for age and metallicity using the mean and the standard deviation of ages and metallicity calculated with pPXF. The simulated population consisted in 1000 galaxies for RCS0327.

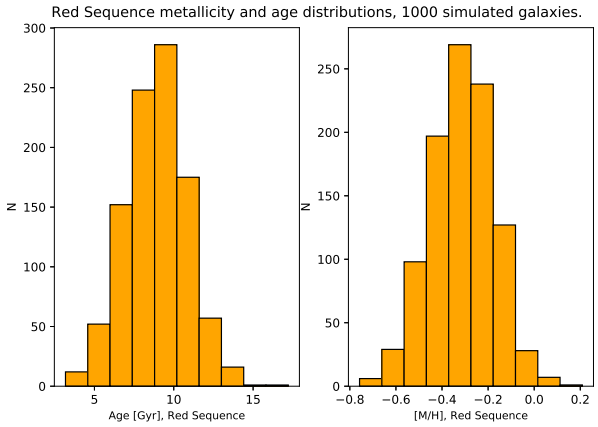

Figure 4.13: Gaussian distribution for age and metallicity from galaxies belonging to the Red Sequence of the cluster. The simulated population consisted in 1000 galaxies for RXJ1347.

The histograms for the ages and metallicities of the simulated galaxy populations are shown in Fig. 4.11 and Fig. 4.12, for both clusters. As stated in Section 4.2, we used the color distributions of these simulated samples to determine 1σ and therefore for setting the limits for the red sequence of each cluster. This is described in the orange lines of the color-magnitude diagrams. So, in this way, the red sequence for each cluster is composed of the galaxies within the orange lines in the color-magnitude diagrams.

Then in order to compare the observable properties of red sequence galaxies (MUSE data), as we did to determine the threshold of the red sequence in each cluster previously explained, we simulated a population of galaxies according to the values of metallicity and ages only of the galaxies belonging to the **red sequence**. This sample was created to compare the colors of the simulated red sequence galaxies using the Charlot & Bruzual color models (see Section 3.4) with the actual color measurements of the galaxies members of the **red sequence** of the clusters.

The age and metallicity distributions of the simulated red sequence galaxies can be seen in Fig. 4.13 and Fig. 4.14. We can see comparing the histogram for the simulated population of all galaxies and red sequence galaxies; there is not a big difference be-

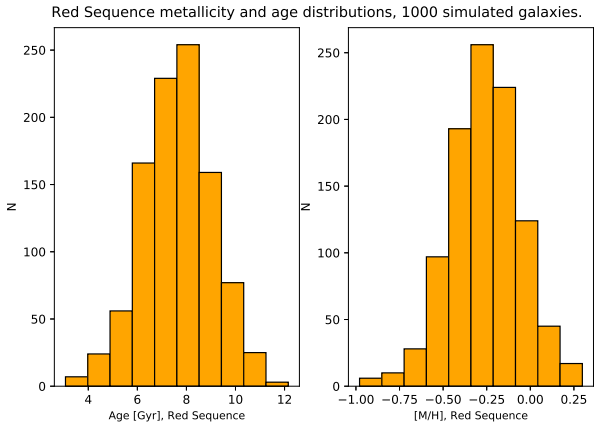

Figure 4.14: Gaussian distribution for age and metallicity from galaxies belonging to the Red Sequence of the cluster. The simulated population consisted in 1000 galaxies for RCS0327.

tween all galaxies and red sequence galaxies. There are slightly older galaxies in the simulated red sequence sample.

An important aspect to consider is that the age and metallicity of the simulated galaxies are randomly paired. This means that we do not follow any rule to assign a particular age and metallicity to a simulated galaxy. We did this according to the real observable measured, as we can see in Fig. 4.7 and Fig. 4.8, we did not find a clear relation between age and metallicity for galaxies in RXJ1347 neither in RCS0327. The usage of the simulated red sequence population is explained in Section 4.4.

4.4 Offset of the Red Sequence

Previous works have studied what drives the slope of the red sequence in clusters of galaxies. Kodama & Arimoto (1997), studying red sequences at different redshifts, discarded the age as a cause of the slope. The other alternative as causative of the slope is metallicity. In our work, we do not see a clear relation between the slope of the red sequence for both clusters and the metallicity of the member galaxies.

Stott et al. (2009) investigated the evolution of the optical and near-infrared color-magnitude relation in a sample of massive clusters from $0 < z < 1$. They found that the rest-frame δ(U-V)/δV slope of the color-magnitude relation evolves with redshift between $z \sim 0.5$ and $z \sim 0.1$, which they ascribe to the build-up of the red sequence over time, showing that the slope of the red sequence increases with redshift. With the values of red sequence slopes for both clusters RCS0327 and RXJ1347, being $\sim$ -0.07 and $\sim$ -0.08, respectively, it is not clear a trend with the slope and redshift. Our sample does not contain enough clusters of galaxies to explore this premise.

As it is appreciated on the CMDs of the clusters, there is a scatter or offset in the fit of the red sequence, i.e. the red sequence galaxies are not equally represented by an identical red sequence fit. These offset from the red sequence fit remains even with high-quality photometry; high-quality photometry does not just signify precision (photometric errors smaller than any intrinsic scatter) but also accuracy, unbias the galaxy photometry, especially faint galaxies. Some investigators (e.g. Romeo et al. (2016); Nishizawa et al. (2017), Connor et al. (2019)) have studied the intrinsic scatter of the red sequence using different techniques.

In this context, we explored the offset of the red sequence in the two clusters. It is essential to mention that the red sequence of each cluster was performed using two different pairs of HST bands. For RXJ1347, we used F475W - F125W, and for RCS0327 F606W - F160W. As we said in the previous section, the selection of these filters was made considering each cluster's redshift, $z = 0.45$ and $z = 0.56$, respectively, so in this way, both clusters are represented by similar colors.

We found that a possible causing of the red sequence offset of a cluster can be related to the relative ages differences of the red sequence galaxy members. In Fig. 4.15 and Fig. 4.16 we present modified color-magnitude diagrams, where the galaxies are colored

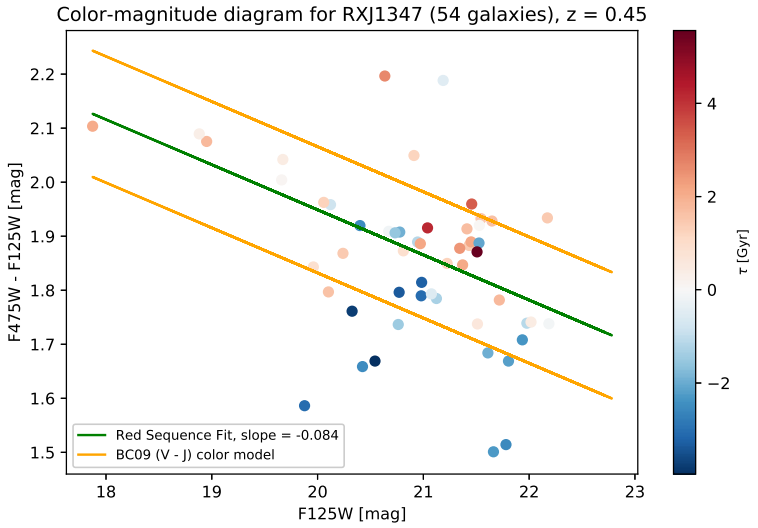

Figure 4.15: Color-magnitude diagram compared to difference to the mean age of the galaxies in the cluster.

by τ, with τ being:

$$\tau = \tau_{gal} - \tau_{m-g} \tag{4.1}$$

Where τ_{gal} is the age of a galaxy and τ_{m-g} is the mean galaxy age of the cluster, considering all the members, not only red sequence galaxies. Negative τ values mean that the respective galaxy is below the mean age of the galaxies in the cluster; therefore, it is younger than the mean age for galaxies in the cluster. Positive τ values correspond to the oldest galaxies in the cluster compared to mean galaxy age. The range of τ is around 8 Gyr for RXJ1347, and 6 Gyr for RCS0327.

We see a relation between the red sequence offset (or color offset) and τ. In both clusters, redder galaxies, i.e galaxies with red sequence offset positive or above the red sequence fit, tend to have higher ages. This effect can be seen more clearly in the RXJ1347 cluster than in RCS0327; one of the reasons for the difference can be the number of galaxies in the sample of each cluster, in the case of RCS0327, the number

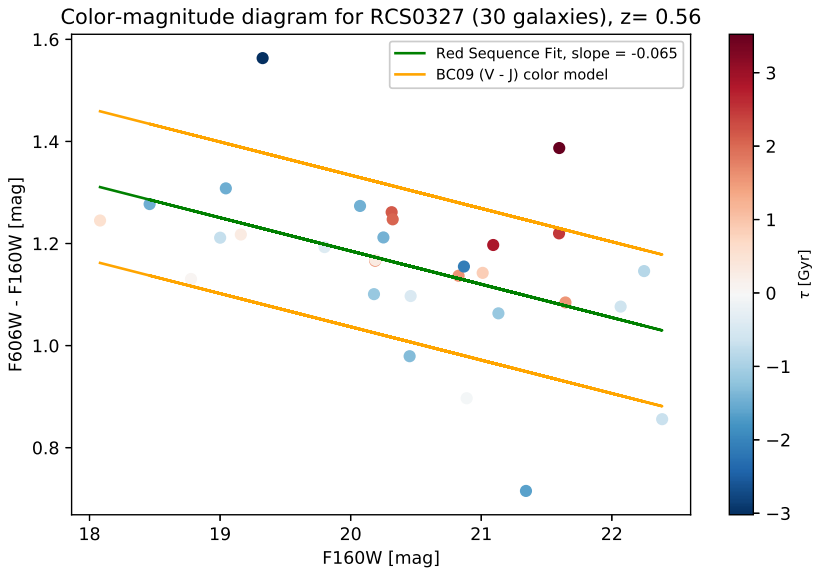

Figure 4.16: Color-magnitude diagram compared to difference to the mean age of the galaxies in the cluster.

is almost the 50% of the RXJ1347 sample.

Now, we analyze the red sequence offset and the relation with τ directly. Fig. 4.17 shows τ as function of the red sequence offset for the two clusters. Red points correspond to RCS0327 galaxies and blue dots to RXJ1327 galaxies. Red sequence offset equal to zero means that the galaxy lies over the red sequence fit of the cluster. Top arrows indicate the range that red sequence covers in each cluster. The black line of the figure corresponds to a linear fit of the galaxies within the red sequence extrapolated to the full range of galaxies. We can see that the fit slope is positive, illustrating an increasing relation between color in the red sequence and age compared to the mean galaxy age of the cluster. In this way, it is possible to say that the red sequence can be tracking the mean age of the galaxies in a cluster at different magnitudes and colors.

As well, as we compare τ with the red sequence offset, we did it with the metallictiy:

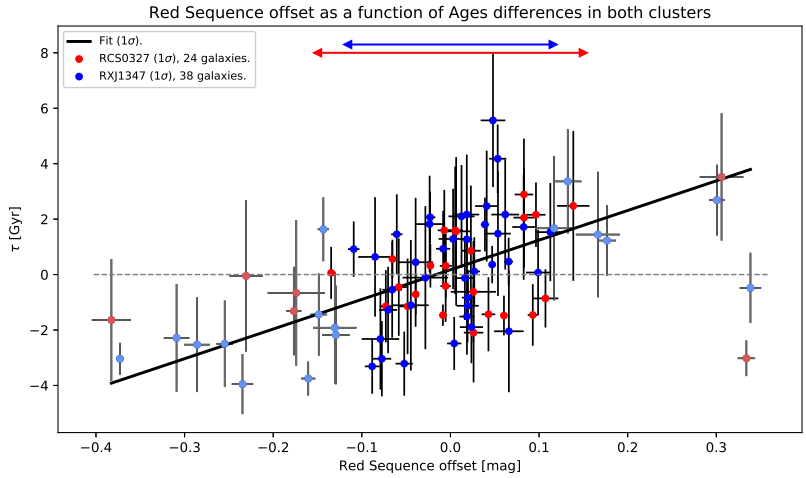

Figure 4.17: Offset in the red sequence compared to τ. τ indicates the galaxy's age compared to the mean galaxy age of its respective cluster. Red dots are galaxies in RCS0327 cluster, and blue dots are galaxies in RXJ1347. Light colors represent galaxies that are outside 1σ (not red sequence galaxies). Red and blue arrows in the top part of the plot indicate the zones that cover 1σ. Black line corresponds to a fit performed only with the galaxies inside 1σ (red sequence galaxies). It is important to note that 1σ is different for both clusters, so to perform the fitting we considered the galaxies inside the respective 1σ region.

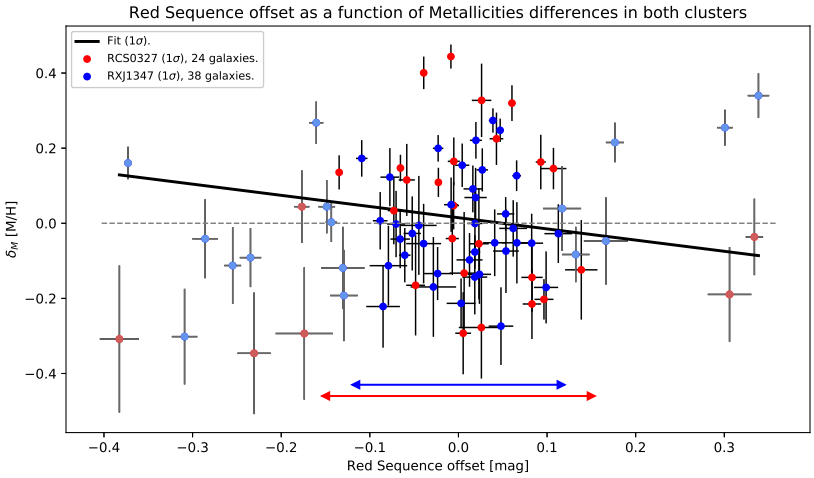

Figure 4.18: Offset in the red sequence compared to δ_M. δ_M indicates the galaxy's metallicity compared to the mean galaxy metallicity of its respective cluster. Red dots are galaxies in RCS0327 cluster, and blue dots are galaxies in RXJ1347. Light colors represent galaxies that are outside 1σ (not red sequence galaxies). Red and blue arrows indicate the zones that cover 1σ. Black line corresponds to a fit performed only with the galaxies inside 1σ (red sequence galaxies). It is important to note that 1σ is different for both clusters, so to perform the fitting we considered the galaxies inside the respective 1σ region.

$$\delta_M = Metal_{gal} - Metal_{m-g} \tag{4.2}$$

Where $Metal_{gal}$ is the metallicity of a galaxy and $Metal_{m-g}$ is the mean galaxy metallicity of the cluster, considering all the galaxies.

In this case, we did not find any clear relation between δ_M and the red sequence offset (see Fig. 4.18).

We compared Fig. 4.17 with color models (see Section 3.4). To accomplish this, we used the simulated populations of red sequence galaxies as it was described in Section 4.3. We performed this analysis in a separated way for each cluster.

We used the same approach described in Section 4.3 to link a color in the (V - J) filter according to a simulated age and metallicity representative of a galaxy. This means that we simulated red sequence galaxies from ages and metallicity of red sequence galaxies in RCS0327 and RXJ1347. As we have seen before, in both clusters, the ages and metallicity of the galaxies seemed not to follow any relation (see Fig. 4.7 and Fig. 4.8). For this reason, we paired a simulated metallicity and age randomly. Thus, the simulated red sequence galaxies have a characteristic age and metallicity that are not connected by any relation. Consequently, we also had to simulate several red sequences to cover all the possible age-metallicity combination space.

We simulated in total 180 red sequences for each cluster. The results of this process can be seen in Fig. 4.19 y Fig. 4.20. In both cases, RXJ1347 and RCS0327, the simulated red sequence galaxies with solar metallicities (shown in red color) are the best representatives of the scatter as a function of the age of the actual galaxies in the cluster, which is described in the plot by the black line. This means that stars with metallicity similar to the Sun can better describe the stellar population of the red

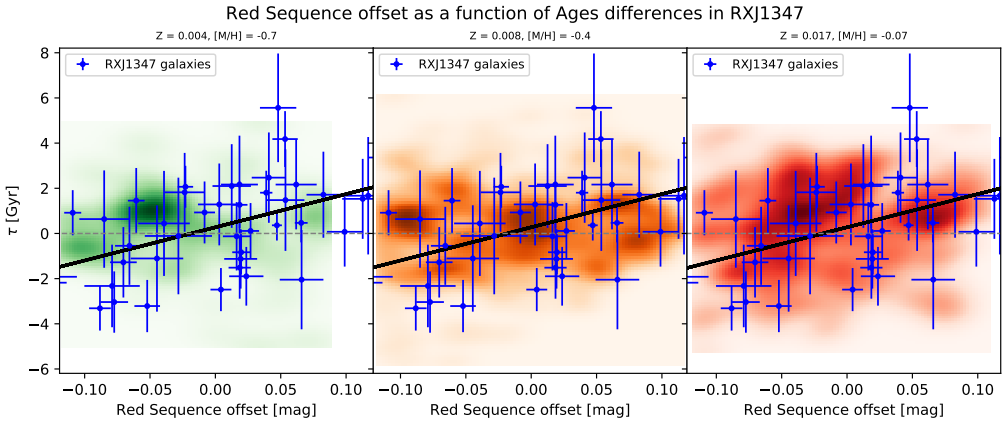

Figure 4.19: Offset in the RXJ1347 red sequence as a function of the ages of the galaxies. Blue dots represent red sequence galaxies in the cluster with respective errors in the parameters. The black line is a fit for the observable data. Simulated galaxies are plotted as a color density map according to the metallicity. Green and orange maps correspond to sub-solar metallicity, while the red map corresponds to solar metallicity.

sequence galaxies in the clusters.

Connor et al. (2019) studied the red sequence galaxies in flour CLASH clusters at z = 0.355 ± 0.007, finding out similar metallicities (~solar) values considering the error values.

While some studies (Arimoto (1996), Kodama & Arimoto (1997)) used the evolution of the red sequence at different redshifts, concluding that metallicity is responsible for the slope of the red sequence, discarding the age; we found that the scatter of the red sequence can be explained mainly as an effect of the different mean ages of the stellar population of the galaxies belonging to it.

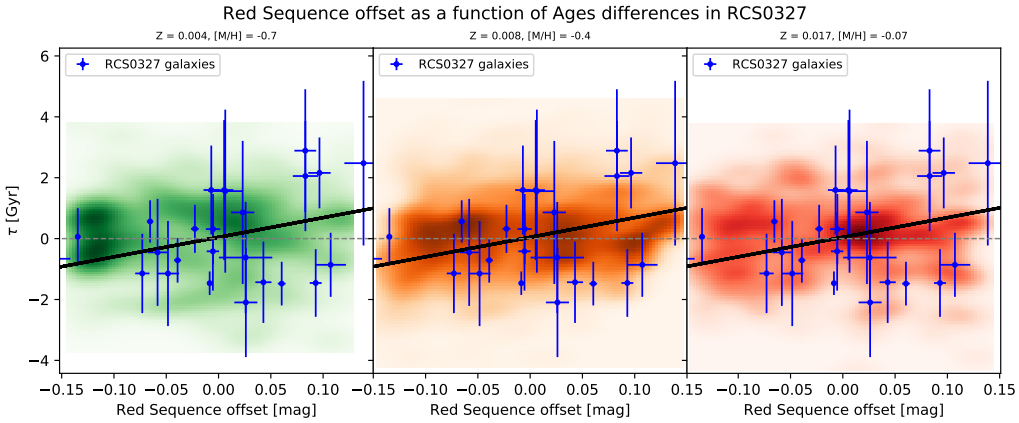

Figure 4.20: Offset in the RCS0327 red sequence as a function of the ages of the galaxies. Blue dots represent red sequence galaxies in the cluster with respective errors in the parameters. The black line is a fit for the observable data. Simulated galaxies are plotted as a color density map according to the metallicity. Green and orange maps correspond to sub-solar metallicity, while the red map corresponds to solar metallicity.

4.5 Cumulative Mass Fraction

As we stated before, we consider that an SSP can describe the stellar population of the galaxies in the clusters. In this sense, we assumed that the galaxies formed the majority of their stellar mass in a major star-forming event. We wanted to study the cosmic history of mass assembly in these systems. Some options to investigate the history of massive early-type galaxies (ETGs) come from the so-called archeological approach, where evolutionary properties at z=0 of ETGs are deduced. Another alternative is the look-back approach, where ETGs progenitors are observed directly at higher redshifts. Various studies suggest an empirical evolutionary trend, named downsizing (Cowie et al. (1996)), where massive galaxies formed earlier and faster than lower mass systems. This last scenario is supported by observational evidence (Dressler et al. (1987), Faber S. M. & Gonzales J. J. (1992)), where they noticed that more massive elliptical galaxies to be more enriched in α-elements than less massive ones (Citro et al. (2016)).

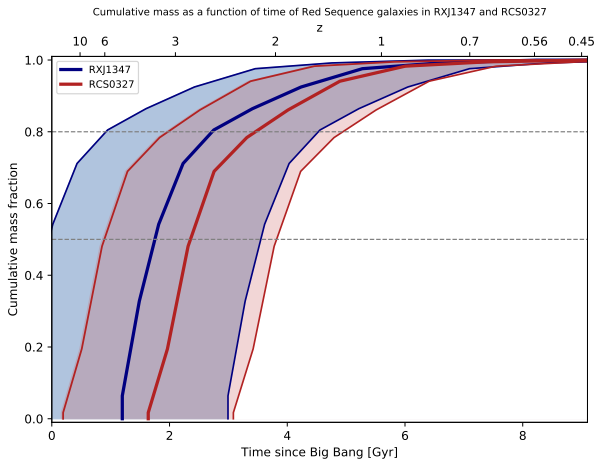

Figure 4.21: Cumulative mass of galaxies as a function of time. RXJ1347 red sequence galaxies (38) are represented in blue and RCS0327 red sequence galaxies (24) in red. Thick and thin lines represent mean values and standard deviation of the cumulative mass fraction for the distribution of each cluster, dotted gray lines represent 50% and 80%.

If we want to give a physical interpretation to these approaches, there are two models to explain ETGs formation, which we will take into account. De Lucia et al. (2006) considered the AGN feedback to quench the star formation earlier in more massive galaxies compared to less massive systems considering the standard scheme of the hierarchical stellar mass assembly. With this in mind, the role of the AGNs is affecting the galaxy evolution and quenching star formation in the systems. On the other hand, the rapid formation of ETGs can be explained by supernova processes. On this matter, massive systems are more efficient in reincorporating gas ejected by supernovae.

Considering this, we studied the cumulative mass fraction of the red sequence galaxies in both clusters as a function of the time. As we have stated before, we considered templates (*E-MILES*) ranging from 1-17 Gyr in the full-spectrum fitting of our galaxies; we normalized the cumulative mass fraction such that the total stellar mass was reached at the redshift of the respective cluster. The result is presented in Fig. 4.21.

In both clusters, most of the galaxies formed around 80% of their stellar mass at z>2. We can infer that the ETGs have gone through a phase of vigorous star formation at pretty early stages of the Universe. With our data and information available, we can picture that these galaxies formed mass very early and too fast for us to be sensitive to the exact time. In this context, the formation timescale for red sequence galaxies are ~1.8 Gyr and ~1.4 Gyr, in RXJ1347 and RCS0327, respectively.

Comparing the galaxies in both clusters, it is possible to see an indication that the red sequence in RCS0327 is formed slightly faster than in RXJ1347. Still, it is important to consider that both samples have a difference ~40% in the number of red sequence galaxies, so this might be a bias effect, owing to we have a higher number of faint galaxies in RXJ1347.

Shetty & Cappellari (2015) studied the star formation history of several galaxies at redshift $0.7 < z < 0.9$, using full-spectrum fitting, with a sample representative of the red sequence and the blue cloud. They found out that the most massive galaxies formed the majority of their stars in the early epoch of the Universe and that the changes in the SFH of the galaxies through time have a dependence on the stellar mass.

If we consider that Type II supernova is the results of explosions of massive stars which live 100 Myr or less and, also that Type II supernovae quickly add gas to the ISM and incorporate it into new stars (Sparke & Gallagher (2007)), as the red sequence galaxies of our sample formed their stellar population very early, possibly Type II supernovae played an important role in polluting the ISM and incrementing the stellar mass of the galaxies rapidly. As the gas ejected by Type II supernova explosions moves slower than Type Ia, it is simpler for the galaxy to retain the gas.

Taking into account De Lucia et al. (2006) results, it is reasonable to think that AGN feedback played a role in the quenching of the red sequence galaxies, even though

we did not explore this scenario in our work.

It would be interesting to explore the evolution of the red sequence of clusters at different redshifts, to see if there is a dependence on how rich is the red sequence of a cluster in terms of number of members and, with the ages and metallicity of the galaxies.

Chapter 5

Conclusions

In this work, we have studied early-type galaxies of two clusters at z= 0.56 and z= 0.45, using full-spectrum fitting with pPXF software and *E-MILES* library. The derived galaxy ages and metallicities indicate that brighter galaxies tend to be more metal-rich and that stellar ages and metallicities are not directly related. We defined the red sequence and its members for both clusters. We found that red sequence galaxies are better described by a stellar population with solar metallicity and also that the offset/scatter of the red sequence relates to the ages of the galaxies compared with the mean galaxy age of the cluster.

The red sequence limits for both clusters are not the same. In the case of RCS0327, red sequence galaxies cover a wider region in the color-magnitude diagram, compare to RXJ1347. This can be a consequence of the fact that the galaxy samples for both clusters do not contain the same number of members. Even so, we see similar behaviors between the red sequence galaxies for both clusters: they are represented by stellar populations with solar metallicities; the red sequence offset undercovers a relation with stellar populations ages of the galaxies, while the metallicities of the populations is not related to the scatter.

We also studied how the red sequence galaxies accumulate stellar mass, and we found that the majority of them have more than 80% of their mass assembled at z>2. Even though we do not have enough sensitivity to establish the exact moment when the galaxies started accumulating their mass, we can state that they began forming stars at the early stages of the Universe, with a time span of ~1.4 or ~1.8 Gyr depending on the cluster. Given the uncertainties it is possible to state that both cluster share a similar history of star formation in their galaxies.

Bibliography

Abell G. O., 1958, ApJS, 3, 211

Abraham R. G., 1998, arXiv e-prints, pp astro–ph/9809131

Allen S. W., Schmidt R. W., Fabian A. C., Ebeling H., 2003, Monthly Notices of the Royal Astronomical Society, 342, 287–298

Arimoto N., 1996, in Leitherer C., Fritze-von-Alvensleben U., Huchra J., eds, Astronomical Society of the Pacific Conference Series Vol. 98, From Stars to Galaxies: the Impact of Stellar Physics on Galaxy Evolution. p. 287

Beifiori A., Maraston C., Thomas D., Johansson J., 2011, Astronomy & Astrophysics, 531, A109

Bernardi M., Renzini A., da Costa L. N., Wegner G., Alonso M. V., Pellegrini P. S., Rité C., Willmer C. N. A., 1998, 508, L143

Bertin E., Arnouts S., 1996, A&AS, 117, 393

Boardman N. F., et al., 2017, Monthly Notices of the Royal Astronomical Society, 471, 4005–4026

Bradač M., et al., 2008, ApJ, 681, 187

Bruzual G., Charlot S., 2003, 344, 1000

Cappellari M., 2017, MNRAS, 466, 798

Cappellari M., Emsellem E., 2004, PASP, 116, 138

Carrasco M., et al., 2017, The Astrophysical Journal, 834, 210

Citro A., Pozzetti L., Moresco M., Cimatti A., 2016, 592, A19

Cohen J., Kneib J.-P., 2001, The Astrophysical Journal, 573

Connor T., Kelson D. D., Donahue M., Moustakas J., 2019, 875, 16

Conroy C., Graves G. J., van Dokkum P. G., 2013, 780, 33

Cowie L. L., Songaila A., Hu E. M., Cohen J. G., 1996, 112, 839

De Lucia G., Springel V., White S. D. M., Croton D., Kauffmann G., 2006, 366, 499

Dressler A., Lynden-Bell D., Burstein D., Davies R. L., Faber S. M., Terlevich R., Wegner G., 1987, 313, 42

Faber S. M. W. G., Gonzales J. J. 1992, The Stellar Populations of Galaxies

Feldmeier-Krause A., Lonoce I., Freedman W. L., 2021, Stellar Population and Elemental Abundance Gradients of Early-type Galaxies (**arXiv:2110.02860**)

Girardi L., Bressan A., Bertelli G., Chiosi C., 2000, A&AS, 141, 371

Gitti M., 2004, Astronomy and Astrophysics, 427

Gitti, M. Ferrari, C. Domainko, W. Feretti, L. Schindler, S. 2007, A&A, 470, L25

Gladders M. D., Yee H. K. C., 2001, in Clowes R., Adamson A., Bromage G., eds, Astronomical Society of the Pacific Conference Series Vol. 232, The New Era of Wide Field Astronomy. p. 126 (**arXiv:astro-ph/0011073**)

González-López R. A., Bruzual-A. G., Charlot S., Ballesteros-Paredes J., Loinard L., 2010, 403, 1213

Gonçalves G., Coelho P., Schiavon R., Usher C., 2020, Monthly Notices of the Royal Astronomical Society, 499, 2327–2339

Kennicutt Robert C. J., 1998, apj, 498, 541

Kodama T., Arimoto N., 1997, 320, 41

Kuiper G. P., 1938, ApJ, 88, 472

Kuntschner H., Smith R. J., Colless M., Davies R. L., Kaldare R., Vazdekis A., 2002, Monthly Notices of the Royal Astronomical Society, 337, 172

Leveque A., 2016-2017, Evolution of galaxies in clusters, unpublished thesis

Lu T., et al., 2010, MNRAS, 403, 1787

Maraston C., Strömbäck G., 2011, MNRAS, 418, 2785

Mo H., van den Bosch F., White S., 2010, Galaxy Formation and Evolution. Cambridge University Press

Morgan W. W., Keenan P. C., Kellman E., 1943, An atlas of stellar spectra, with an outline of spectral classification

Nishizawa A. J., et al., 2017, Publications of the Astronomical Society of Japan, 70

Ota, N. et al., 2008, A&A, 491, 363

Pessa I., Tejos N., Moya C., 2018, PyMUSE: a Python package for VLT/MUSE data (arXiv:1803.05005)

Romeo A. D., Cerulo P., Xi K., Contini E., Sommer-Larsen J., Gavignaud I., 2016, The high-redshift evolution of the Red Sequence scatter from joint simulations and HAWK-I Cluster Survey (arXiv:1611.04671)

Salpeter E. E., 1955, ApJ, 121, 161

Sánchez-Blázquez P., et al., 2006, MNRAS, 371, 703

Schindler S., et al., 1995, A&A, 299, L9

Schmidt M., 1959, apj, 129, 243

Shetty S., Cappellari M., 2015, Monthly Notices of the Royal Astronomical Society, 454, 1332

Sparke L. S., Gallagher John S. I., 2007, Galaxies in the Universe

Stott J. P., Pimbblet K. A., Edge A. C., Smith G. P., Wardlow J. L., 2009, Monthly Notices of the Royal Astronomical Society, 394, 2098

Tremonti C. A., et al., 2004, apj, 613, 898

Vazdekis A., Casuso E., Peletier R. F., Beckman J. E., 1996, ApJS, 106, 307

Vazdekis A., Sánchez-Blázquez P., Falcón-Barroso J., Cenarro A. J., Beasley M. A., Cardiel N., Gorgas J., Peletier R. F., 2010a, Monthly Notices of the Royal Astronomical Society

Vazdekis A., Sánchez-Blázquez P., Falcón-Barroso J., Cenarro A. J., Beasley M. A., Cardiel N., Gorgas J., Peletier R. F., 2010b, MNRAS, 404, 1639

Worthey G., Trager S. C., Faber S. M., 1995, in Buzzoni A., Renzini A., Serrano A., eds, Astronomical Society of the Pacific Conference Series Vol. 86, Fresh Views of Elliptical Galaxies. p. 203

Wright E. L., 2006, PASP, 118, 1711

Wuyts E., et al., 2010, The Astrophysical Journal, 724, 1182–1192

Zahid H. J., Geller M. J., Fabricant D. G., Hwang H. S., 2016, ApJ, 832, 203

Zahid H. J., Sohn J., Geller M. J., 2018, ApJ, 859, 96

Zwicky F., Herzog E., Wild P., Karpowicz M., Kowal C. T., 1961, Catalogue of galaxies and of clusters of galaxies, Vol. I

Appendices

A Stellar Population gradients in Galaxies

As we explained in Section 2.3.4, we divided the galaxies into two parts: an internal circular region and an outer ring-shaped region, both containing approximately equal sum of light.

Having two spectra for each galaxy, using pPXF, we computed the respective ages and metallicity of both regions, obtaining in this way gradients. In Fig. 1 we can see the metallicity and age gradients for 13 galaxies and 25 galaxies in RCS0327 and RXJ1347, respectively. M_{grad} denotes the metallicity gradient and t_{grad} the age gradient, defined as:

$$M_{grad} = M_{in} - M_{out} \tag{1}$$

$$t_{grad} = t_{in} - t_{out} \tag{2}$$

where the subscript ***in*** are parameters for the internal region of each galaxy and the subscript ***out*** are parameter for the external ring-shaped region.

It is important to mention that these parameters are light-weighted. Having said this, we can see a metallicity gradient for the galaxies in both clusters, where the internal or central part is more metal-rich than the outer part of the galaxy. The age

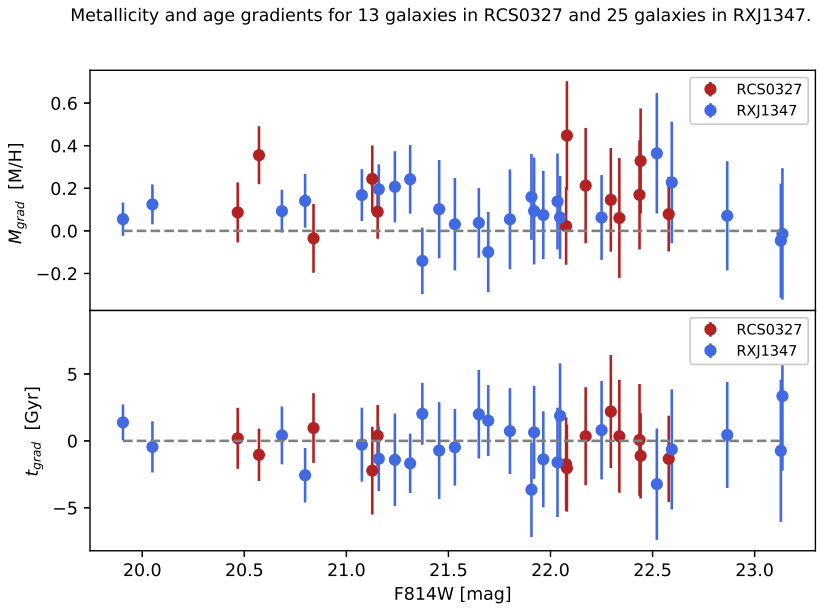

Figure 1: Metallicity and age gradients for both clusters. Red and blue dots correspond to galaxies in RCS0327 and RXJ1347, respectively. The top panel corresponds to the metallicity gradient and the lower panel to the age gradient, both as a function of the apparent magnitude in the F814W HST band.

gradient is not that evident; the ages tend to be more homogeneous in the two apertures for the galaxies. We also can see that ages are poorly constrained for faint galaxies.

Feldmeier-Krause et al. (2021) studied the galaxy gradients radius up to $1R_e$ in 8 early-type galaxies at z~0. They used optical spectroscopy and full-spectral fitting to measure stellar population age, metallicity, and other properties. They found ages ranging from 3–13 Gyr. They found negative [Z/H] gradients and a decreasing or constant age. It is important to take into account that they studied galaxies in the local Universe. Also, they performed gradients analysis radially and did not consider all the light of the galaxies.

Other research (Boardman et al. (2017)) observed 12 nearby HI-detected early-type galaxies extracting Lick index measurements of the frequently used Hβ , Fe5015, Mg b, Fe5270, and Fe5335 absorption features. They found most galaxies to have flat Hβ

gradients and negative Mg b gradients. They measured gradients (up to 3 times the central effective radius) of age, metallicity, and abundance ratio for the galaxies using spectral fitting. In most of the galaxies, they found negative age and metallicity gradients.

It will be interesting to compare these results with age and metallicity gradients computed with a similar technique but in clusters of galaxies at a wide redshift range. With a more significant cluster sample, we could study how the gradients evolve with time and what it can tell us about the formation processes and scales of the galaxies at different redshifts.

B Full-spectrum fitting results

Here we present pPXF outcomes for all (not only red sequence) the galaxies in RXJ1347 and RCS0327 for regularized and unregularized weights. These results come from full-spectrum fitting, and it was performed in the spectrum that considers "100%" of galaxy light. Error estimations come from Monte Carlo simulations.

Table 1: Stellar population results for galaxies in RXJ1347. ID is the identification for each galaxy, RA is the right ascension, and Dec is the declination, both degrees. The apparent magnitude in the HST band F814W, velocity dispersion (σ), age t (regularized/unregularized), total metallicity $[Z/H]$ (regularized/unregularized), and their respective errors are also presented. The parameters are light-weighted.

	ID	RA	Dec	F814W [mag]	σ [km/s]	σ error [km/s]	t [Gyr]	t error [Gyr]	[Z/H]	[Z/H] error	t [Gyr] unregul	[Z/H] unregul
1	4891_4239	206.88472	-11.75950	21.7	132.6	10.6	7.1	1.5	-0.26	0.07	6.7	-0.24
2	4881_3713	206.88480	-11.74721	22.9	40.1	11.1	6.2	1.8	-0.42	0.11	7.1	-0.45
3	4067_6436	206.89173	-11.74119	21.2	160.8	14.6	10.0	1.4	-0.39	0.07	10.5	-0.42
4	6972_4385	206.86700	-11.75827	22.9	70.2	16.7	7.5	2.4	-0.31	0.13	7.7	-0.30
5	6679_3651	206.86950	-11.76440	22.0	121.9	12.6	7.4	1.3	-0.24	0.08	7.8	-0.26
6	4700_4947	206.88635	-11.75359	21.9	112.9	8.7	5.5	1.4	-0.18	0.08	5.3	-0.17
7	5128_5152	206.88270	-11.75189	20.9	241.3	11.7	8.7	1.2	-0.16	0.06	8.5	-0.18
8	5817_5740	206.87683	-11.74698	23.1	92.2	16.8	10.0	2.3	-0.35	0.12	10.4	-0.37
9	4977_3546	206.88398	-11.76527	21.4	160.6	8.8	6.1	1.0	-0.15	0.06	6.2	-0.15
10	5861_3061	206.87646	-11.76931	22.0	97.6	9.8	10.7	2.2	-0.45	0.10	10.8	-0.44
11	5881_6047	206.87629	-11.74443	22.5	169.7	20.8	10.0	2.2	-0.38	0.11	9.7	-0.36
12	6314_3291	206.87260	-11.76740	20.0	245.2	8.9	10.4	1.0	-0.03	0.03	10.1	-0.03
13	5901_4153	206.87612	-11.76021	21.7	210.7	10.3	11.3	1.3	-0.05	0.05	11.0	-0.04
14	5329_5221	206.88099	-11.75131	22.0	122.7	14.1	7.3	1.6	-0.31	0.09	7.4	-0.31
15	6101_5490	206.87442	-11.74907	21.6	117.4	9.2	8.4	1.5	-0.21	0.06	8.8	-0.21
16	5139_4995	206.88260	-11.75319	18.9	323.8	8.8	10.6	0.9	-0.11	0.04	10.1	-0.09
17	4980_4776	206.88396	-11.75502	20.8	202.8	5.9	5.5	0.6	-0.14	0.04	5.4	-0.14
18	3696_5332	206.89489	-11.75039	20.9	183.9	6.7	9.5	1.0	-0.13	0.05	9.1	-0.14
19	6246_5713	206.87318	-11.74721	21.5	65.4	11.2	6.1	1.6	-0.42	0.10	6.5	-0.44
20	5488_3794	206.87964	-11.76320	21.9	181.9	10.6	9.8	1.3	-0.09	0.05	9.4	-0.10
21	6088_4798	206.87453	-11.75484	22.4	149.3	19.5	10.3	1.9	-0.36	0.08	10.2	-0.37
22	6027_3990	206.87505	-11.76157	19.9	283.7	12.0	8.9	0.7	-0.06	0.03	9.1	-0.06
23	5633_4497	206.87840	-11.75734	22.0	177.3	12.6	12.7	1.2	-0.28	0.04	12.5	-0.28
24	6027_3232	206.87505	-11.76789	22.3	134.7	13.9	11.0	2.0	-0.36	0.09	11.0	-0.37
25	5755_3610	206.87736	-11.76474	21.8	95.6	10.5	6.7	1.3	-0.44	0.08	7.0	-0.42
26	5601_3176	206.87867	-11.76835	22.3	102.2	14.4	10.7	1.9	-0.40	0.07	11.0	-0.42
27	5444_4371	206.88001	-11.75840	22.7	92.1	13.9	10.4	1.7	-0.44	0.07	10.0	-0.42
28	4885_4182	206.88477	-11.75997	22.0	109.8	8.5	8.0	1.7	-0.35	0.08	8.0	-0.35
29	6349_5307	206.87231	-11.75060	22.4	106.4	12.1	10.7	2.0	-0.32	0.08	10.8	-0.32
30	4312_6259	206.88964	-11.74266	21.2	207.7	11.1	7.7	1.0	-0.08	0.05	7.8	-0.10
31	5369_5010	206.88065	-11.75307	22.5	106.1	18.7	6.3	1.9	-0.61	0.13	5.6	-0.56
32	6048_4724	206.87487	-11.75545	21.0	142.5	7.2	10.2	1.2	-0.30	0.05	9.7	-0.30
33	5703_4031	206.87780	-11.76123	21.5	107.8	14.0	4.6	1.1	-0.40	0.08	4.7	-0.37
34	5309_5021	206.88116	-11.75298	22.6	108.1	18.7	6.5	2.2	-0.36	0.11	6.1	-0.32
35	6298_4506	206.87274	-11.75727	22.7	63.4	13.8	6.4	1.8	-0.50	0.12	6.5	-0.50
36	5546_3995	206.87915	-11.76153	21.7	143.9	15.5	5.3	1.0	-0.30	0.08	5.1	-0.29
37	6452_5997	206.87143	-11.74485	22.5	135.1	11.9	10.1	1.8	-0.33	0.08	10.5	-0.36
38	4018_5626	206.89214	-11.74794	22.5	68.2	13.8	9.2	2.2	-0.53	0.11	9.0	-0.52
39	5124_2840	206.88274	-11.77115	21.9	122.7	12.1	5.4	1.2	-0.33	0.10	5.5	-0.32
40	5719_5438	206.87767	-11.74951	22.2	109.8	17.0	9.9	1.8	-0.52	0.07	9.2	-0.48
41	5723_6253	206.87763	-11.74271	22.6	46.0	11.4	6.7	2.0	-0.42	0.11	6.6	-0.38
42	6299_5336	206.87273	-11.75035	22.4	119.3	15.9	11.9	1.9	-0.39	0.07	10.7	-0.35
43	4842_5244	206.88514	-11.75112	20.7	207.6	8.1	9.0	0.9	-0.18	0.04	9.2	-0.19
44	6494_5453	206.87108	-11.74938	23.1	86.9	18.1	8.5	2.6	-0.47	0.13	7.7	-0.45
45	4609_4879	206.88712	-11.75416	22.5	67.8	14.3	14.1	2.4	-0.58	0.10	13.8	-0.59
46	4687_2892	206.88646	-11.77072	21.1	169.3	10.4	9.8	1.0	-0.38	0.04	10.0	-0.39
47	5311_3443	206.88114	-11.76613	21.7	139.8	10.7	7.1	1.4	-0.31	0.08	7.2	-0.31
48	4800_5489	206.88549	-11.74908	22.7	99.8	18.5	10.2	2.6	-0.27	0.11	9.7	-0.25
49	3949_4394	206.89274	-11.75820	22.9	101.2	15.1	9.0	2.3	-0.36	0.11	8.6	-0.34
50	7020_5560	206.86660	-11.74848	21.3	111.8	5.8	4.8	0.6	-0.04	0.06	4.8	-0.04
51	4159_5136	206.89095	-11.75202	22.6	83.3	12.8	6.0	1.7	-0.35	0.11	5.9	-0.35
52	4003_5311	206.89228	-11.75056	21.7	173.1	11.9	9.5	1.4	-0.26	0.07	9.4	-0.27
53	5274_5627	206.88145	-11.74793	22.2	216.2	18.5	8.1	1.3	0.04	0.06	8.3	0.04
54	5000_3493	206.88379	-11.76571	22.6	216.8	26.9	8.6	1.5	-0.48	0.10	8.6	-0.48

Table 2: Stellar population results for galaxies in RCS0327. ID is the identification for each galaxy, RA is the right ascension, and Dec is the declination, both degrees. The apparent magnitude in the HST filter F814W, velocity dispersion (σ), age t (regularized/unregularized), total metallicity $[Z/H]$ (regularized/unregularized), and their respective errors are also presented. The parameters are light-weighted.

	ID	RA	Dec	F814W [mag]	σ [km/s]	σ error [km/s]	t [Gyr]	t error [Gyr]	[Z/H]	[Z/H] error	t [Gyr] unregul	[Z/H] unregul
1	899_899	51.86351	-13.43882	20.5	350.2	15.0	8.0	0.7	-0.16	0.04	8.1	-0.16
2	738_1152	51.86533	-13.43605	24.0	77.5	35.0	6.8	1.8	-0.58	0.14	7.8	-0.65
3	814_725	51.86447	-13.44075	22.6	159.4	22.1	9.6	1.2	-0.51	0.05	9.6	-0.52
4	739_661	51.86532	-13.44145	23.7	54.7	48.2	7.4	2.7	-0.65	0.16	7.1	-0.63
5	374_1018	51.86945	-13.43752	23.0	185.6	21.4	10.3	2.0	-0.52	0.09	9.1	-0.49
6	224_934	51.87115	-13.43845	20.6	352.5	12.0	6.0	0.4	0.14	0.03	5.9	0.12
7	759_718	51.86510	-13.44083	23.1	300.7	25.1	6.6	1.1	-0.16	0.06	6.9	-0.18
8	1122_943	51.86099	-13.43835	22.2	212.8	16.5	6.3	1.3	-0.27	0.09	6.5	-0.26
9	929_747	51.86318	-13.44050	23.8	100.5	26.2	5.8	2.2	-0.61	0.20	4.2	-0.51
10	1511_1164	51.85659	-13.43591	22.9	162.8	32.8	8.3	2.3	-0.36	0.15	8.7	-0.33
11	1284_474	51.85916	-13.44350	20.8	317.5	26.7	7.5	0.9	-0.17	0.05	7.5	-0.16
12	663_781	51.86618	-13.44013	23.0	142.6	22.2	6.3	1.7	-0.47	0.13	6.1	-0.44
13	414_173	51.86900	-13.44682	21.4	241.6	16.3	4.4	0.6	-0.34	0.10	4.1	-0.33
14	643_553	51.86641	-13.44263	22.3	133.2	13.3	6.1	1.6	-0.26	0.10	6.4	-0.26
15	179_574	51.87166	-13.44241	24.1	51.3	39.8	6.8	2.6	-0.60	0.18	5.8	-0.58
16	761_569	51.86507	-13.44247	21.1	263.7	10.6	6.0	0.7	0.01	0.05	5.7	0.03
17	962_934	51.86280	-13.43844	21.9	355.7	36.8	7.0	1.3	-0.26	0.06	7.0	-0.26
18	848_774	51.86409	-13.44021	22.4	231.9	19.3	9.1	1.5	-0.35	0.10	9.4	-0.35
19	603_977	51.86687	-13.43797	22.3	137.4	11.3	6.0	1.3	-0.08	0.07	6.4	-0.09
20	880_1184	51.86373	-13.43570	22.7	184.7	36.0	9.1	2.3	-0.60	0.11	9.4	-0.61
21	119_1107	51.87234	-13.43654	23.5	150.9	34.3	9.0	2.7	-0.44	0.16	7.9	-0.43
22	806_833	51.86457	-13.43955	22.8	166.2	18.0	9.5	1.8	-0.45	0.09	10.8	-0.47
23	555_213	51.86740	-13.44638	22.1	155.2	14.5	7.8	1.2	-0.14	0.06	7.5	-0.12
24	746_610	51.86524	-13.44201	23.7	151.0	38.1	11.0	2.3	-0.49	0.13	10.9	-0.51
25	24_868	51.87342	-13.43917	22.8	148.7	23.4	5.4	1.8	0.02	0.10	5.5	0.00
26	1374_738	51.85814	-13.44060	23.4	99.2	26.7	9.9	2.7	-0.43	0.13	11.0	-0.46
27	658_1004	51.86624	-13.43767	22.1	230.3	16.3	6.0	1.1	-0.14	0.07	6.1	-0.14
28	1555_446	51.85609	-13.44381	21.0	325.6	23.3	6.7	0.7	0.10	0.04	7.0	0.10
29	775_724	51.86491	-13.44075	21.2	272.4	18.0	7.8	0.8	-0.20	0.04	8.7	-0.24
30	1205_1099	51.86005	-13.43662	22.4	176.6	14.7	7.0	1.8	-0.19	0.10	6.9	-0.18